

## Article

# Alkaline Silicate Metasomatism Recorded through Fe-Ti-Rich Mantle Xenoliths from the Calatrava Volcanic Field (Spain)

Javier García Serrano <sup>1</sup>, Carlos Villaseca <sup>1,2,\*</sup>, Cecilia Pérez-Soba <sup>1</sup> and Manuel Jesús Román-Alpiste <sup>3</sup>

<sup>1</sup> Departamento de Mineralogía y Petrología, Facultad de Ciencias Geológicas, Universidad Complutense de Madrid, C/José Antonio Novais 12, 28040 Madrid, Spain; jgserrano@ucm.es (J.G.S.); pesoa@ucm.es (C.P.-S.)

<sup>2</sup> Instituto de Geociencias IGEO (UCM, CSIC), C/Doctor Severo Ochoa 7, 28040 Madrid, Spain

<sup>3</sup> Instituto Andaluz de Ciencias de la Tierra, CSIC-Universidad de Granada, Av. de las Palmeras, 4, Armilla, 18100 Granada, Spain; mj.roman@csic.es

\* Correspondence: granito@geo.ucm.es

**Abstract:** Much of the lithospheric subcontinental mantle (SCLM) sampled in the Calatrava Volcanic Field (CVF) shows refertilization by alkaline metasomatic agents. The Cerro Pelado and El Palo ultramafic xenolith suites record the best evidence of this type of metasomatism in this volcanic field. Several groups of peridotite (lherzolite, wehrlite, and dunite) and pyroxenite (clinopyroxenite and websterite) xenoliths have been distinguished. Despite having scarce phlogopites and amphiboles as modal metasomatic phases, all studied xenoliths present a variable cryptic metasomatism, highlighted by the strong Fe-Ti enrichment and fractionated REE patterns in the most evolved wehrlite and pyroxenite varieties. They show a common trend of an Fe-Ti-Ca increase, whereas the pyroxenites are more depleted in Fe compared to the lherzolites and wehrlites. Trace-element (REE and multi-trace) patterns are roughly similar among them, suggesting different interactions and refertilization degrees by alkaline silicate melts. The same Sr-Nd isotopic EAR composition, combined with trace-element chemistry of metasomatic xenolith phases and phenocrysts from the Calatrava volcanics, highlights the main role of this magmatism in percolation processes beneath Central Iberia. These mantle xenoliths also show variable amounts of interstitial glass that originated by in situ partial melting, favored by the enriched chemical nature of cryptically metasomatized clinopyroxene during their volcanic transport. This alkaline-refertilized mantle type represents the main domain within the SCLM beneath Central Iberia, as was also recorded in other Western European Cenozoic volcanic fields.

**Keywords:** alkaline metasomatism; peridotite xenoliths; pyroxenite xenoliths; Fe-Ti-rich wehrlites; websterite xenolith; subcontinental lithospheric mantle



**Citation:** García Serrano, J.; Villaseca, C.; Pérez-Soba, C.; Román-Alpiste, M.J. Alkaline Silicate Metasomatism Recorded through Fe-Ti-Rich Mantle Xenoliths from the Calatrava Volcanic Field (Spain). *Minerals* **2024**, *14*, 241. <https://doi.org/10.3390/min14030241>

Academic Editor: Alexandre V. Andronikov

Received: 23 January 2024  
Revised: 19 February 2024  
Accepted: 23 February 2024  
Published: 27 February 2024



**Copyright:** © 2024 by the authors. Licensee MDPI, Basel, Switzerland. This article is an open access article distributed under the terms and conditions of the Creative Commons Attribution (CC BY) license (<https://creativecommons.org/licenses/by/4.0/>).

## 1. Introduction

The mantle xenoliths exhumed by Cenozoic alkaline volcanoes are an essential source of information about the nature and evolution of the subcontinental lithospheric mantle (SCLM) [1]. Therefore, ultramafic xenoliths brought to the surface by alkaline and ultra-alkaline magmas of the Calatrava Volcanic Field (CVF) represent a probe of the SCLM composition under the central part of the Iberian Peninsula. Previous studies in the CVF [2–8] have identified spinel-bearing lherzolites, with scarce or negligible evidence of refertilization as the primordial lithospheric mantle [9,10].

Nevertheless, many other CVF peridotite xenoliths show evidence of having undergone subsequent metasomatic interactions. A small number of xenoliths have undergone subduction metasomatism [10], whereas most xenolith suites record subsequent refertilization by alkaline metasomatism. This last metasomatism, which is considerably more extended, has compositional characteristics that are typical of interactions with carbonatite or carbonate-rich alkaline melts [4,7] or with undersaturated silicate melts, as previously recorded for xenoliths from the Cerro Pelado and El Palo volcanoes [3,11].

Much of the SCLM sampled in the European Cenozoic volcanic fields shows metasomatic interactions through silicate alkaline melts [12,13]. In this work, we characterize a large data set of ultramafic xenoliths from the El Palo and Cerro Gordo volcanic centers that show evidence of having been refertilized by silicate alkaline metasomatic agents, generating different lithological varieties: Fe-Ti-rich lherzolites and wehrlites, metasomatic dunites, and pyroxenite (clinopyroxenite and websterite) xenoliths (Figure 1). These last types are rare in other xenolith suites of the CVF.

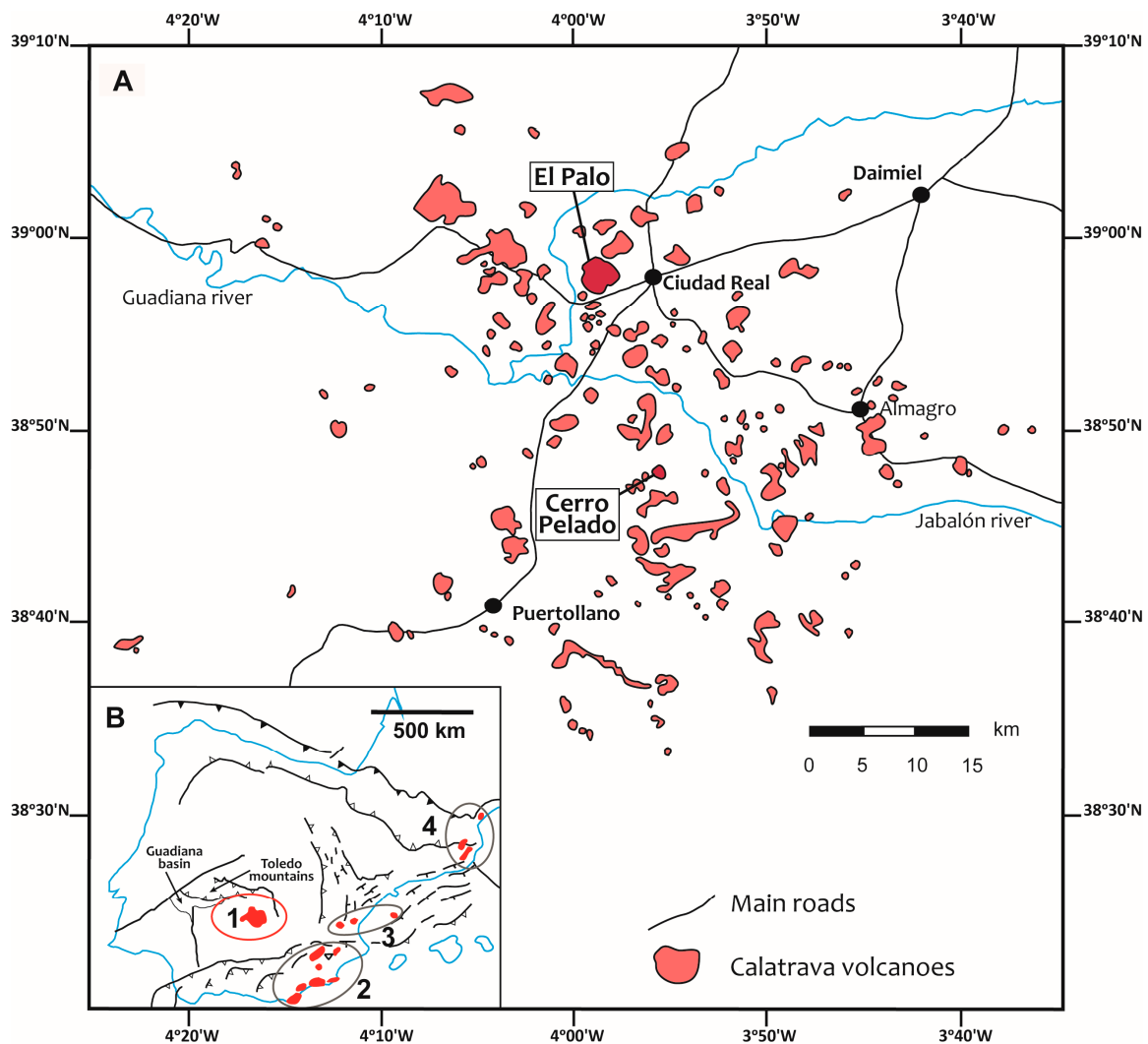


**Figure 1.** (A) Geological sketch map of the Calatrava Volcanic Field and location of the Cerro Pelado and El Palo volcanoes (modified from [14,15]). (B) Sketch map of the Iberian Peninsula showing the location of the Cenozoic volcanic fields in Spain [16]: (1) Calatrava or central region; (2) SE region; (3) Levante region; and (4) Olot or NE region.

## 2. Geological Setting

Alkaline mafic magmas erupted in different regions of Western and Central Europe during the Cenozoic times, defining the Circum-Mediterranean Anorogenic Cenozoic Igneous Province (CiMACI [17]). The CVF represents an anorogenic intracontinental alkaline magmatic zone formed in recent Cenozoic times within the CiMACI. This volcanic field is located at the western termination of the SSW–NNE tectonic basin of the Guadiana River, bordered to the north-west by the Toledo Mountains (Figure 1). The CVF was constructed over a Paleozoic basement that was later uplifted during the Alpine orogeny [18,19]. The NNW–SSE distribution of Calatrava volcanic vents is mainly conditioned by old Variscan shear bands reactivated by the Betic collision [15]. The geodynamic setting of the Calatrava volcanism is

still controversial, with the debate focused on three main models: (1) volcanic clustering related to asthenospheric-mantle upwelling (hot spots or diapiric instabilities) in a pre-rifting stage [20,21]; (2) a megafault system affecting the western Mediterranean European block [19]; and (3) mantle instabilities in a back-arc position during the roll-back of the Alboran slab [22,23].

The CVF is formed mainly by monogenetic volcanic centers, suggesting small and short-lived magma chambers. This volcanic field consists of more than 250 volcanic centers [21] in an area of around 5500 km<sup>2</sup>. Most edifices are strombolian cones, although more than 80 tuff rings and maars, and scarce lava flows, have also been described. The volcanic activity of the CVF began in the Late Miocene, defining two different stages. The first stage was a minor ultrapotassic event around 7.4 to 7.1 Ma ago [21], forming the leucititic Morrón de Villamayor volcano. The second and main stage, from 4.3 to 0.7 Ma [21], was dominated by Na-rich alkaline magmas, generating basanite, olivine melilitite, and nephelinite volcanoes, including the two that have been studied in this work: El Palo and Cerro Pelado.

Peridotite xenoliths appear in a scarce number of these three types of volcanic edifices. Most of them are spinel-bearing lherzolites, whereas other lithological types (e.g., dunite, wehrlite, and pyroxenite xenoliths) are less abundant and have only been found in some centers (e.g., El Aprisco, El Palo, Cerro Pelado, and Los Tormos). The two studied volcanoes (Cerro Pelado and El Palo, Figure 1) are strombolian cones, in which mantle xenoliths occur within the pyroclastic fall deposits. Nevertheless, the El Palo volcano is a polygenetic complex that was mainly destroyed by aggregate quarry industries and was flattened and progressively restored due to their proximity to the city of Ciudad Real. Thus, the sampling of mantle xenoliths in this volcano has been performed in the debris accumulates around the demolished scoria cones. In the near future, this debris will probably be covered.

### 3. Methods

Twenty-five ultramafic xenoliths from the Cerro Pelado and El Palo volcanoes were selected for this study. The modal xenolith composition was estimated by point-counting (1629–932 points per thin section). Significant errors in their classification by this method may be considered, as some mantle xenoliths are small and are compositionally banded.

The major-element mineral composition was analyzed at the Centro Nacional de Microscopía Electrónica (Complutense University of Madrid, Spain) using a Jeol JXA-8900 M electron microprobe (Jeol Ltd., Yokyo, Japan) with four wavelength-dispersive spectrometers. Analytical conditions were an accelerating voltage of 15 kV and an electron beam current of 20 nA, with a beam diameter of 5 µm. Elements were counted for 10 s on the peak and 5 s on each background position. Corrections were made using an online ZAF method. Detection limits were 0.02 wt% for Al, Na, K, and P; 0.03 wt% for Ti, Fe, Mn, and Mg; Ni and Cr; and 0.04 wt% for Si. Error limits for each element depended strongly on the absolute concentration in each phase but could be estimated significantly for the <1 wt% level (with error > 10%). Concentrations below 0.2 wt% were quoted but considered qualitative. Mineral analyses were assisted by appropriate back-scattered electron (BSE) images to ensure that representative and homogeneous points were selected for analysis.

We determined the in situ concentrations of 30 trace elements (REE, Ba, Rb, Sr, Th, U, Nb, Ta, Pb, Zr, Hf, Y, Sc, V, Co, Zn, and Cr) in mineral grains on >60 µm-thick polished sections using laser ablation (LA-ICPMS) at the Instituto Andaluz de Ciencias de la Tierra (CSIC) of Granada, using an Agilent 8800 QQQ ICP-MS (Agilent Technologies CO., Ltd., Santa Clara, CA, USA) coupled to a Photon Machines Analyte Excite 193 laser source (Teledyne Photon Machines, Bozeman, MT, USA). The diameter of the laser beam was from 40 to 85 µm (depending on the mineral size), associated with repetition rates of 10 Hz and laser fluence at the target of ca. 8 J/cm<sup>2</sup>. A 0.8 L/min He flow was used on the laser system to transport the nebulized material to the ICP-MS, where a 1.2 L/min Ar flow was used as a carrier to introduce the nebulized material into the plasma. A 40–30 s gas blank was analyzed first to establish the background, followed by 60 s measurements

for the remainder of the analysis. On the ICPMS side, a dwell time of 0.1 ms was used to acquire the major element masses, while a dwell time of 2 ms was used to obtain the rest of the masses. The NIST 611 glass was used as a primary reference material to calibrate relative element sensitivities for analyses of the silicate minerals. Precision and accuracy were assessed from repeated analyses of the USGS-BIR 1G and BHVO-2G reference materials (Supplementary Table S1) and are estimated to be between 2% and 10% for most of the analyzed trace elements. Each analysis was normalized to Si or Ca as Internal Standards using concentrations determined by the electron microprobe. The Iolite V2.5 software [24] was used for data reduction through the Trace-Element Data-reduction Scheme [25]. REEView add-on was used to determine the correct time interval on each analysis to avoid impurities, contamination, or inclusions.

The whole-rock major and trace-element compositions were analyzed at ACTLABS. Samples were melted using  $\text{LiBO}_2$  and were dissolved with  $\text{HNO}_3$ . The solutions were analyzed by inductively coupled plasma atomic emission spectrometry (IACP-AES) for major elements, whereas trace elements were determined by ICP mass spectrometry (ICP-MS). Uncertainties in major elements were bracketed between 1 and 3%, except for Mn (5%–10%) and  $\text{P}_2\text{O}_5$  (>10%). The precision of the ICP-MS analyses at low concentration levels (trace elements) was evaluated from repeated analyses of the international standards BR, DR-N, UB-N, AN-G, and GH. The precision for Rb, Sr, Zr, Y, V, Hf, and most of REE was in the range of 1%–5%, whereas it ranged from 5% to 10% for the rest of the trace elements, including Tm. Some samples had concentrations of certain elements below detection limits ( $\text{K}_2\text{O}$ , 0.01%; Rb, 1; Zr, 1; Nb, 0.2; Tb, 0.01; Ho, 0.01; Tm, 0.005; Lu, 0.002; Hf, 0.01; Ta, 0.01; Th, 0.05; and U, 0.01). More information on the procedure, precision, and accuracy of ACTLABS ICP-MS analyses is available at <https://actlabs.com>.

Sr–Nd isotope ratios were measured at the Centro de Asistencia a la Investigación (CAI) de Geocronología y Geoquímica Isotópica of the Complutense University of Madrid, using an automated Phoenix-IsotopX Multicollector thermal ionization mass spectrometer, with the data acquired in multi-dynamic mode. Whole-rock samples and the separated clinopyroxene were dissolved in ultra-pure reagents, and the isotopes were subsequently isolated by exchange chromatography. The analytical procedures used in this laboratory are described elsewhere [26]. Repeated analyses on the NBS-987 standard gave  $^{87}\text{Sr}/^{86}\text{Sr} = 0.710240 \pm 0.00005$  ( $2\sigma$ ,  $n = 8$ ) and for the La Jolla standard, and values of  $^{143}\text{Nd}/^{144}\text{Nd} = 0.511847 \pm 0.00003$  ( $2\sigma$ ,  $n = 14$ ) were obtained. The  $2\sigma$  internal analytical errors were 0.01% for  $^{87}\text{Sr}/^{86}\text{Sr}$  and 0.006% for  $^{143}\text{Nd}/^{144}\text{Nd}$ .

## 4. Results

### 4.1. Petrography of Mantle Xenoliths

The studied ultramafic xenoliths from the Cerro Pelado and El Palo volcanoes show a wide variability in their mineral mode (Table 1 and Figure 2). Among them, lherzolites are dominant, but there are also other lithological varieties that draw different compositional trends: wehrlites, dunites, olivine clinopyroxenites, clinopyroxenites s.s., and one websterite (Figure 2). The lherzolites were classified into two groups according to chemical composition (Table 1). Most of these xenoliths display a coarse-grained protogranular texture, except for some fine-grained equigranular varieties and one porphyroclastic lherzolite from El Palo, where porphyroclasts are mainly orthopyroxene (Table 1). El Palo clinopyroxenites, contrary to igneous clinopyroxenite, cumulate from other Calatrava volcanoes [27,28], lack chemically zoned mafic minerals, and their amphibole and phlogopite modal amounts are nil or in trace contents.

**Table 1.** Modal composition and textural features of the Cerro Pelado and El Palo ultramafic xenoliths.

Sample	Volcano	Texture	Calculated Modal Abundances (vol%)						
			OI	Opx	Cpx	Spl	Phl	Amp	Glass
<b>Lherzolites-g1</b>									
117202	El Palo	Prg	52.6	22.0	18.2	4.5	-	-	2.6
117207	El Palo	Prg	52.5	20.1	22.2	3.0	-	-	2.2
117219	El Palo	Prg	66.9	9.5	19.7	2.5	-	-	1.5
117487	El Palo	Pfc	39.5	38.3	18.1	4.0	-	-	0.1
<b>Lherzolites-g2</b>									
65290	Cerro Pelado	Prg	54.4	25.5	17.7	1.9	-	-	0.5
65294	Cerro Pelado	Eq	57.5	17.9	22.5	2.0	-	-	0.1
65298	Cerro Pelado	Prg	60.7	22.8	14.9	1.5	0.1	-	-
111642	Cerro Pelado	Prg	52.6	25.8	16.1	5.2	-	-	0.2
111645	Cerro Pelado	Prg	55.8	16.7	19.9	4.1	1.4	0.9	1.2
111652	Cerro Pelado	Prg	63.3	23.4	9.7	3.0	-	-	0.6
117215	El Palo	Prg	54.8	30.1	12.1	2.9	-	-	<0.1
117483	El Palo	Prg	48.9	25.9	21.3	3.9	-	-	<0.1
117484	El Palo	Pfc	59.7	22.6	14.9	2.8	-	-	<0.1
117486	El Palo	Prg	39.2	37.3	19.3	4.2	-	-	<0.1
117491	Cerro Pelado	Eq	63.1	25.6	7.5	2.6	0.9	-	0.2
<b>Metasomatic dunites</b>									
111640	Cerro Pelado	Prg	87.2	-	3.8 *	-	7.9	-	1.1
111648	Cerro Pelado	Prg	91.2	-	4.5 *	0.4	2.4	-	1.5
<b>Wehrlites</b>									
72674	Cerro Pelado	Prg	69.7	1.4	27.5 *	0.1	0.1	-	1.2
110856	Cerro Pelado	Prg	61.6	-	30.2 *	-	6.1	-	2.1
116604	Cerro Pelado	Eq	53.3	-	43.0 *	1.8	-	-	1.8
117203	El Palo	Eq	55.6	-	41.9	1.6	-	-	0.9
<b>Websterite</b>									
117205	El Palo	Prg	-	55.8	42.1	1.4	-	-	0.6
<b>Olivine Clinopyroxenites</b>									
117480	El Palo	Eq	13.1	-	85.4	-	-	-	1.6
117482	El Palo	Prg	14.8	-	84.7	-	-	-	0.5
<b>Clinopyroxenites</b>									
117217	El Palo	Prg	9.3	-	88.8	-	<0.1	-	1.9
117485	El Palo	Prg	8.7	-	88.5	-	-	-	2.8

Prg = coarse-grained protogranular; Pfc = porphyroclastic; Eq = fine-grained equigranular; Ol = olivine; Opx = orthopyroxene; Cpx = clinopyroxene; Spl = spinel; Phl = phlogopite; Amp = amphibole; \* = partially or fully recrystallized.

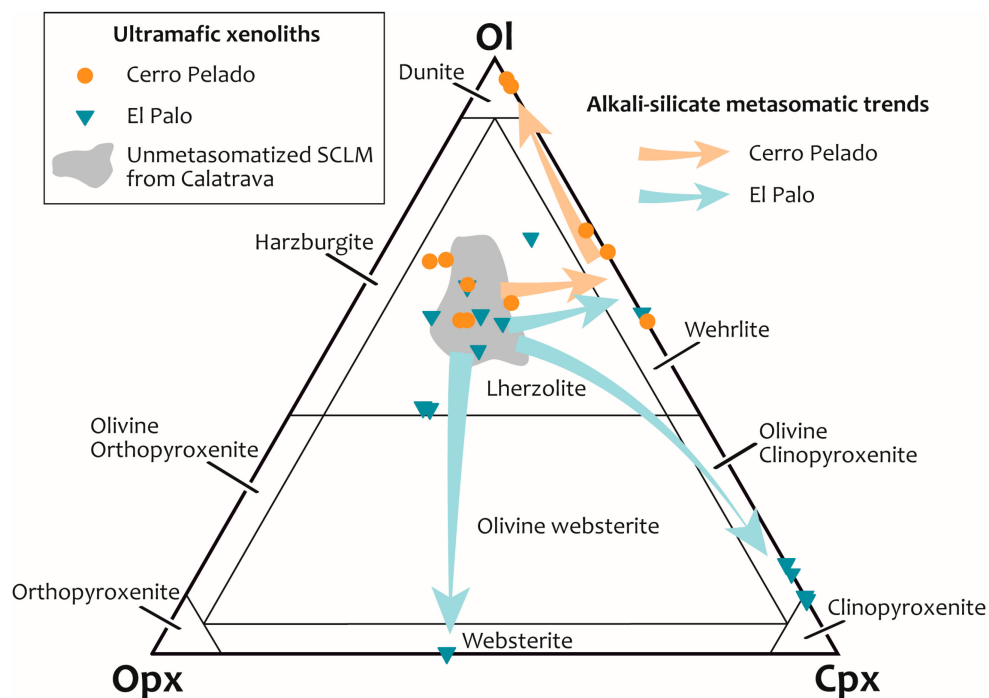


**Figure 2.** Modal proportions of the Cerro Pelado and El Palo mantle xenoliths. Arrows are evolutionary trends of progressive alkaline metasomatism, according to [29].

The main minerals of studied xenoliths are olivine, orthopyroxene, clinopyroxene, spinel, and, occasionally in the more evolved xenoliths, phlogopite and scarce amphibole (as metasomatic minerals) (Table 1). Wehrlites and dunites do not contain orthopyroxene, except in wehrlite 72674 (1.4 modal%, Table 1). Although no harzburgite varieties appear in these mantle xenolith suites, many of the lherzolites and the El Palo websterite have high orthopyroxene contents (up to 56 modal%).

Olivines, in the studied xenoliths, have relatively straight rims among them, and while in contact with other mafic minerals, they show more irregular contacts (Figure 3a–c). Occasionally, olivine shows microcrystals or sub-grains, along with undulating extinction, that suggest intracrystalline deformation, such as those described in other Calatrava xenoliths [6]. Olivine from clinopyroxenites is small in size and shows strong hydrothermal alterations (iddingsite) when close to the xenolith rims (Figure 3d). Orthopyroxene in lherzolites-g2 is usually subhedral and shows larger sizes than the other mafic minerals. However, in lherzolites-g1 and in the wehrlite 72674, orthopyroxene crystals are small with very irregular rims that suggest dissolution (Figure 3c). Orthopyroxene in the websterite is larger than in clinopyroxenites and locally shows intergrowth with clinopyroxene (Figure 4a). Clinopyroxene in lherzolites is anhedral (Figure 3a–d) and shows spongy-textured sectors in reaction zones (Figure 4b). In the wehrlites, dunites, and some of the clinopyroxenites, clinopyroxene presents a highly developed spongy texture affecting either crystal rims (Figures 3 and 4c) or defining neo-formed interstitial crystals (Figure 3b,c). Spinel appears in all lherzolites but is scarcer or absent in the more metasomatized xenoliths (Table 1). Spinel in lherzolites shows a typical holly-leaf shape (Figure 3a), whereas in the wehrlites are microglobular inclusions within the spongy clinopyroxene (Figure 4c).

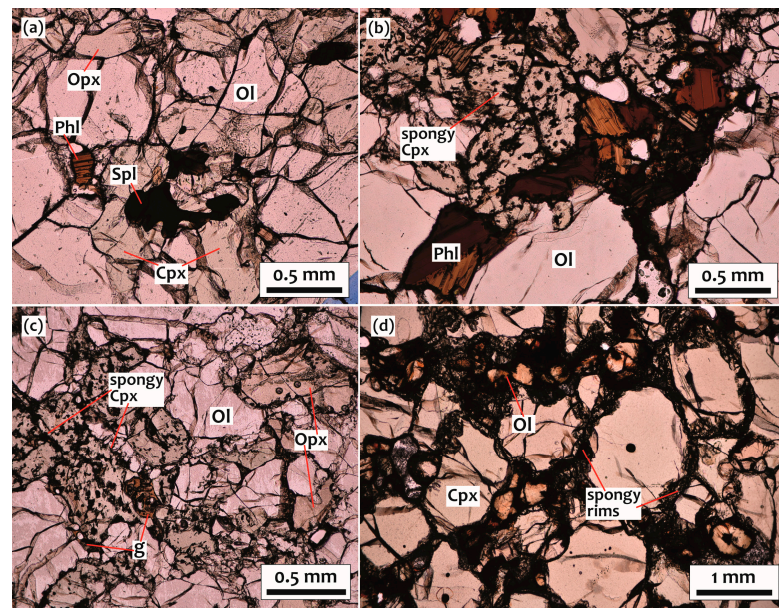


**Figure 3.** Photomicrographs of Cerro Pelado and El Palo mantle xenoliths. (a) Protogranular Cerro Pelado lherzolite-g2 65,298 showing olivine, orthopyroxene, clinopyroxene, accessory phlogopite, and holly-leaf spinel; (b) phlogopite between spongy clinopyroxene and olivine in the Cerro Pelado wehrlite 110856; (c) orthopyroxene corroded crystals associated with recrystallized spongy clinopyroxene and interstitial glass in the Cerro Pelado wehrlite 72674; (d) clinopyroxene crystals with spongy rims in the El Palo olivine clinopyroxenite 117480. Mineral abbreviations are from [30].

The metasomatic minerals in these xenoliths are phlogopites, present mainly in wehrlite and dunite xenoliths from the Cerro Pelado volcano, and scarce amphiboles in one xenolith of this volcanic center (Table 1). Accessory phlogopites also appear in a clinopyroxenite s.s. from the El Palo volcano (Table 1). The phlogopite appears as isolated crystals (Figure 3a) or forming small clusters (Figure 3b), whereas the rare amphibole occurs as interstitial microcrystals (Figure 4e).

In most of these mantle xenoliths, especially in the most evolved types (wehrlites and pyroxenites), it is worth noting the presence of glass, interstitial to the main mafic minerals (Table 1 and Figures 3c and 4b,d,f). This interstitial glass is more abundant in El Palo lherzolites-g1 than lherzolites-g2 (Table 1), being one of the criteria for this lherzolite classification. Interstitial glass occurs as disconnected veins and melt pockets of short length, showing abundant glass vesiculation (vacuoles) (Figure 4b,d,f). Moreover, the secondary microcrysts of olivines, clinopyroxenes, and spinels appear within these melt domains, wherein they highlight acicular neoblastic clinopyroxene crystals (Figure 4b), suggesting fast metastable crystallization. Much of the interstitial glass is altered to zeolites, displaying a cracked and porous appearance (Figure 4d).

#### 4.2. Whole-Rock Composition

##### 4.2.1. Major and Trace Elements

The whole-rock major- and trace-element compositions of the Cerro Pelado and El Palo mantle xenoliths are reported in Supplementary Table S2. The small size of the dunites prevented them from being analyzed.

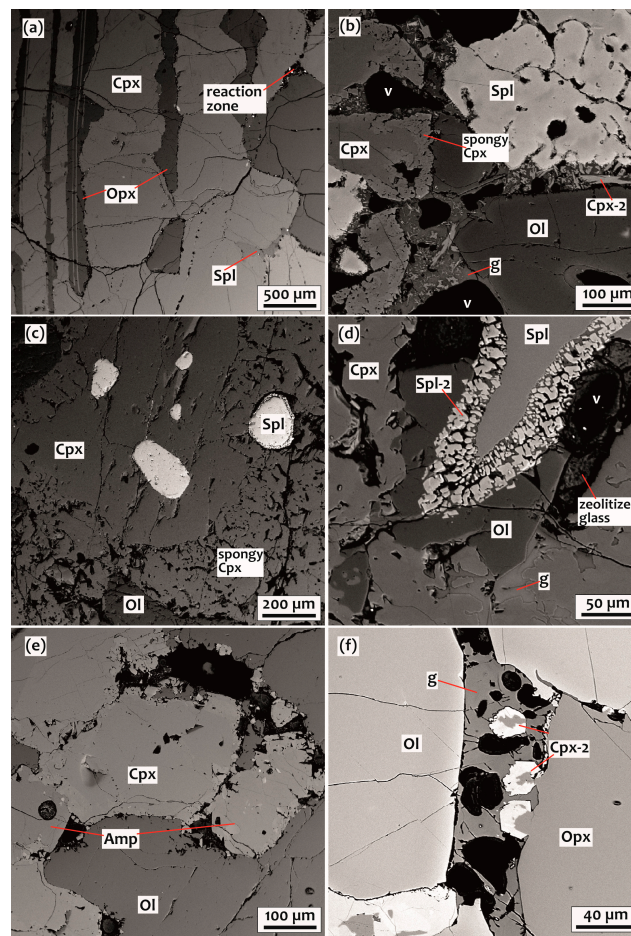


**Figure 4.** BSE micrographs of representative Cerro Pelado and El Palo mantle xenoliths. (a) Orthopyroxene-clinopyroxene intergrowths in the El Palo websterite 117205; (b) spongy clinopyroxene and spinel crystals in contact with a reaction zone that presents interstitial glass and elongated secondary clinopyroxene crystals (Cpx-2) in the El Palo lherzolite-g1 117202; (c) spongy clinopyroxene with spinel inclusions in the El Palo wehrlite 117203; (d) large spinel crystal that presents a spongy rim towards interstitial glass in the El Palo lherzolite-g2 1,172019; (e) interstitial amphibole in the Cerro Pelado lherzolite-g2 111645; (f) interstitial glass with degassed bubbles or vesicles and secondary clinopyroxene neoblasts surrounding residual orthopyroxene cores in the Cerro Pelado wehrlite 72674. Mineral abbreviations are from [30].

Harker diagrams show that peridotite xenoliths have a varied major element composition (Figure 5). The compositional field of unmetasomatized lherzolites of the CVF [9,10] was included as the protolithic SCLM beneath Calatrava (Figure 5). Lherzolites, including those previously sampled in El Palo [2], have compositions close to the primitive mantle and the unmetasomatized lithospheric protolith of Calatrava. The different groups of lherzolites and wehrlites display a negative correlation of MgO with respect to CaO, FeO<sub>t</sub>, and TiO<sub>2</sub> and a positive correlation with respect to Ni (Figure 5). Lherzolites-g1 have a higher TiO<sub>2</sub> and FeO<sub>t</sub> content than lherzolites-g2, drawing on the compositional trend studied in other volcanic centers, towards Fe-Ti-rich wehrlites [12] (Figure 5b,c).

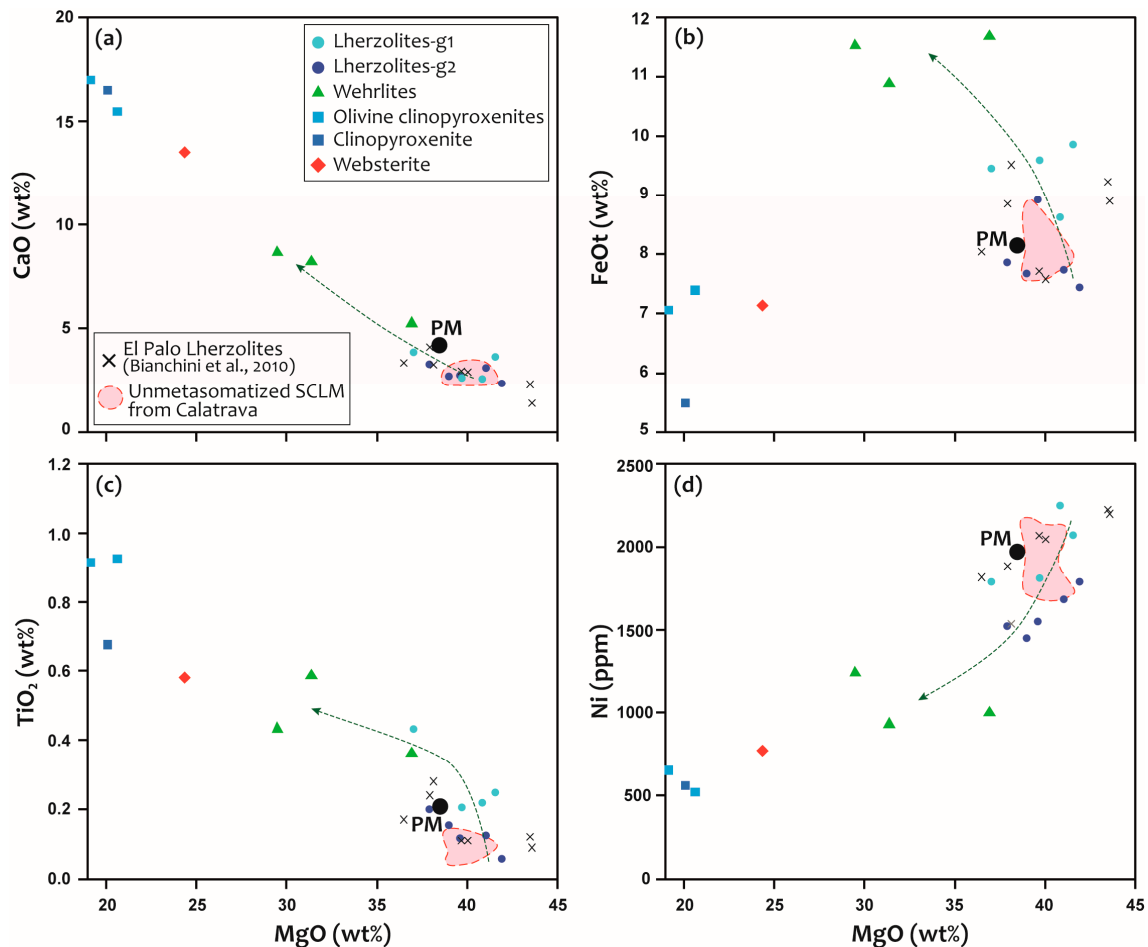


**Figure 5.** Harker diagrams showing variations in whole-rock major oxides (a: CaO, b: FeO<sub>t</sub>, c: TiO<sub>2</sub>) and trace elements (d: Ni) versus MgO (wt%) of the Cerro Pelado and El Palo ultramafic xenoliths. Data of Calatrava unmetasomatized SCLM [9,10] and previously published El Palo xenoliths [2] are shown for comparison. The composition of the primitive mantle [31] is represented by a filled circle. Chemical trends of the Fe-Ti wehrlites are shown.

Pyroxenitic mantle xenoliths have low FeO, MgO, and NiO contents and higher ones in the rest of the major elements (CaO, Al<sub>2</sub>O<sub>3</sub>, SiO<sub>2</sub>, and TiO<sub>2</sub>) (Figure 5 and Table S2), defining more evolved compositions than the set of peridotites. The composition of the websterite is mostly intermediate between that of the lherzolites and that shown by the clinopyroxenites (Figure 5). Pyroxenites are not always projected, in line with the wehrlitic-evolution trend (as in, e.g., FeO<sub>t</sub> content, Figure 5b), but the websterite is always located in positions close to the clinopyroxenite group, linking the wehrlitic evolutions in those diagrams where both fields are aligned (Figure 5a,c,d).

Trace-element composition of these ultramafic xenoliths shows a marked REE enrichment in the chondrite-normalized diagrams (Figure 6a,c). The two groups of lherzolites (and those included in [2]) display similar LREE contents, although lherzolites-g1 have a lower HREE content than lherzolites-g2, showing more fractionated patterns (Figure 6a). Moreover, lherzolites-g1, in multi-trace diagrams, do not display a negative Ti anomaly and have a slight LILE (Rb, Ba, and Sr) and HFSE (Th, U, Nb, Ta, Pb, Zr, and Hf) enrichment with respect to lherzolites-g2 (Figure 6b).

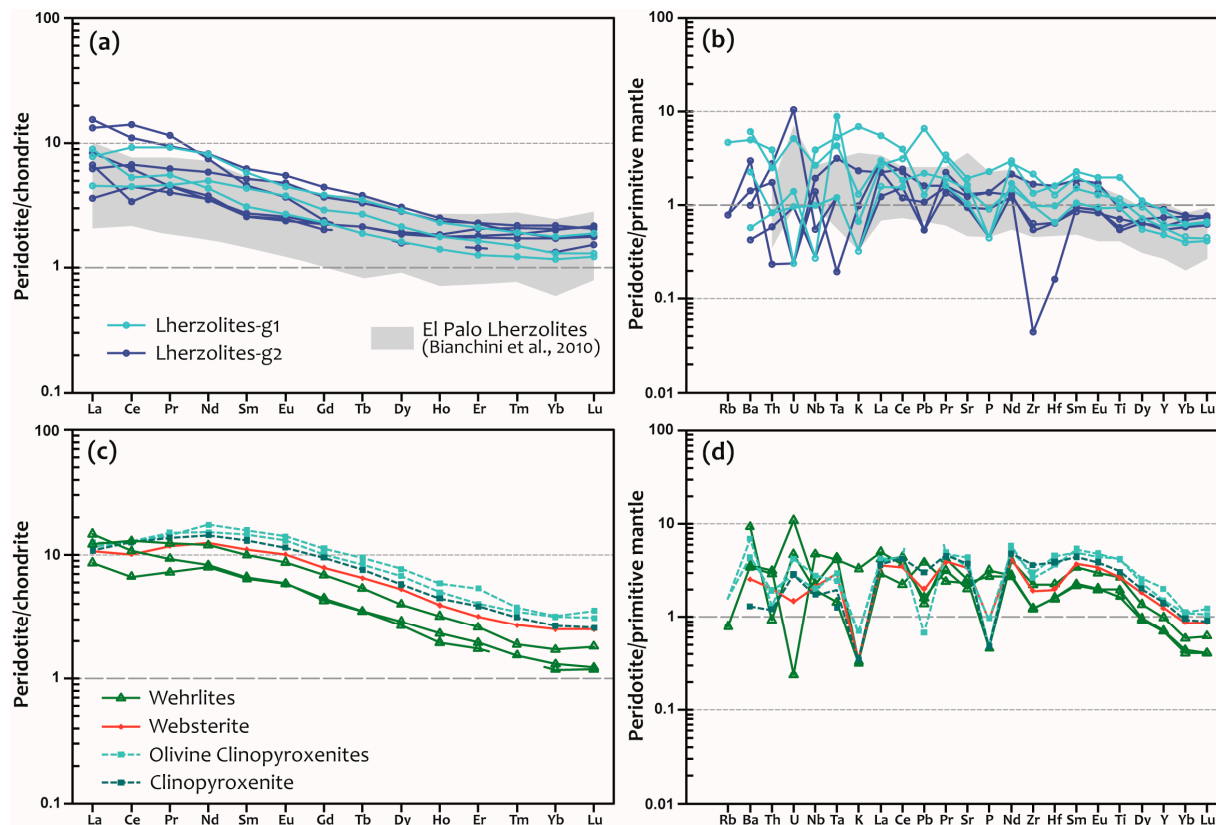


**Figure 6.** Whole-rock chondrite-normalized REE (a,c) and primordial mantle-normalized trace element (b,d) diagrams of the Cerro Pelado and El Palo ultramafic xenoliths. The previously studied El Palo lherzolite compositional field (grey) [2] (is also included for comparison. Normalizing values are from [31].

Wehrlites have similar LREE and HREE contents than lherzolites, but due to their greater MREE enrichment, they show more fractionated REE patterns (Figure 6c). These evolved peridotites have multi-trace patterns that are similar to each other; are smoother than those of the lherzolites; and are with a more marked fractionation into less incompatible elements (from Ti to Lu), due to their great Ti enrichment (Figure 6d).

Pyroxenitic xenoliths show regular and parallel REE and multi-trace-element patterns, which are slightly convex in REE, and have the highest MREE contents. The websterite presents lower values in most trace elements than clinopyroxenites (Figure 6c,d). Pyroxenitic REE patterns are less fractionated than those of the wehrlites due to their higher HREE content (Figure 6c).

#### 4.2.2. Sr–Nd Isotopes

Whole-rock isotopic data of the peridotite and pyroxenite xenoliths of the Cerro Pelado and El Palo volcanoes (initial ratios calculated at the age 2.2 Ma, [7]) are collected in Supplementary Table S3 and are represented in Figure 7. There are no relevant differences between the different ultramafic xenolith groups, and a large part of them overlap with the isotopic compositional field of the Calatrava volcanic rocks (Figure 7). Nevertheless, the studied ultramafic rocks define a wider isotopic compositional field than Calatrava magmas (Figure 7). This suggests a slightly more enriched character of the Calatrava xenoliths when compared to mantle sources of the host alkaline volcanic magmas. This enriched isotopic signature is remarkable when compared to mantle xenoliths from other Iberian Cenozoic intraplate alkaline volcanic fields (e.g., the Olot area [32]), which plot towards a depleted-mantle composition (Figure 7).

The Cerro Pelado and El Palo mantle xenoliths have a wide compositional range, although most of them, except for the wehrlite 117203, have a geochemical affinity with the EAR component [33], also called the common mantle reservoir (CMR) of the CIMACI province [17] (Figure 7), and some of them show affinities to the HIMU source of ocean island basalts (OIBs). The isotopic composition of these ultramafic xenoliths is far from the compositional field of the lherzolite unmetasomatized Calatrava SCLM [9,10], which defines a kind of mixing mantle array between the DM compositional fields (MORB-type) and the EMII component, although with slightly higher  $^{87}\text{Sr}/^{86}\text{Sr}$  ratios (Figure 7).

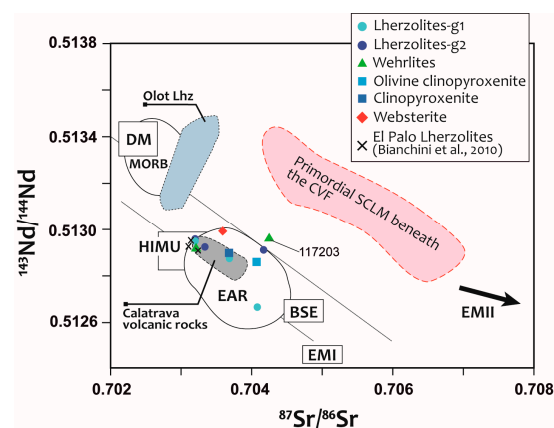


**Figure 7.** Sr–Nd isotope variation diagram for peridotite and pyroxenite xenoliths from the Cerro Pelado and El Palo volcanoes compared to the primordial SCLM from Calatrava [9,10]. Sr–Nd isotopic data from El Palo peridotite xenoliths of [2] are also plotted. Isotopic data of the Calatrava volcanic rocks are from [19,34]. Mantle end members are from [35], except for the EAR domain [33].

#### 4.3. Mineral Chemistry

The mineral composition of the Cerro Pelado and El Palo mantle xenoliths is summarized in Supplementary Tables S4 (major elements) and S5 (trace elements).

##### 4.3.1. Major-Element Mineral Composition

In the Cerro Pelado and El Palo peridotite xenoliths, primary olivine shows a higher Mg# [ $100 \times \text{Mg}^{2+} / (\text{Mg}^{2+} + \text{Fe}^{2+})$  on a molecular basis] in lherzolites (87.3–91.3, especially in lherzolites-g2), than in clinopyroxenites (86.6–87.9), wehrlites (83.7–87.6), and dunites (83.9–85.3) (Figure 8a). Primary lherzolitic olivine also displays higher NiO content than in wehrlites, dunites and clinopyroxenites (Figure 8a). The secondary olivine (associated with glass) shows lower NiO contents compared to the primary one (Figure 8a).

Orthopyroxene shows a similar Mg# range than associated olivine (e.g., in wehrlite 72674:  $\text{Mg}\#\text{Ol} = 84.52\text{--}86.01$ ;  $\text{Mg}\#\text{Opx} = 85.01\text{--}86.59$ ), being higher in lherzolites than in wehrlites (Figure 8b). Although lherzolites-g2 have slightly higher  $\text{Al}_2\text{O}_3$  content than lherzolites-g1, the lherzolite 117491 is the sample with the lowest  $\text{Al}_2\text{O}_3$  content (Figure 8b). The only wehrlite with orthopyroxene (sample 72674) has lower  $\text{Al}_2\text{O}_3$  and higher  $\text{TiO}_2$  contents than orthopyroxene from lherzolite xenoliths (Figure 8b; Table S4). On the other hand, orthopyroxene from the websterite shows the highest  $\text{Al}_2\text{O}_3$  content of the studied xenolith suite, with intermediate Mg# values between the wehrlites and lherzolites (Figure 8b).

Primary clinopyroxene in lherzolites-g2 has slightly higher Mg# and  $\text{Al}_2\text{O}_3$  (but lower  $\text{TiO}_2$ ) contents than those of lherzolites-g1, except for the lherzolite 117491, whose clinopyroxene stands out for its lower  $\text{Al}_2\text{O}_3$  (as happens with orthopyroxene) and higher  $\text{Na}_2\text{O}$  and  $\text{Cr}_2\text{O}_3$  contents (Figure 9). The apparent primary clinopyroxene of wehrlites and dunites shows a more evolved composition than that of the lherzolites, with lower Mg#,  $\text{Cr}_2\text{O}_3$ ,  $\text{Al}_2\text{O}_3$ , and  $\text{Na}_2\text{O}$  (as well as higher  $\text{FeO}$  and  $\text{TiO}_2$ ) contents (Figure 9).

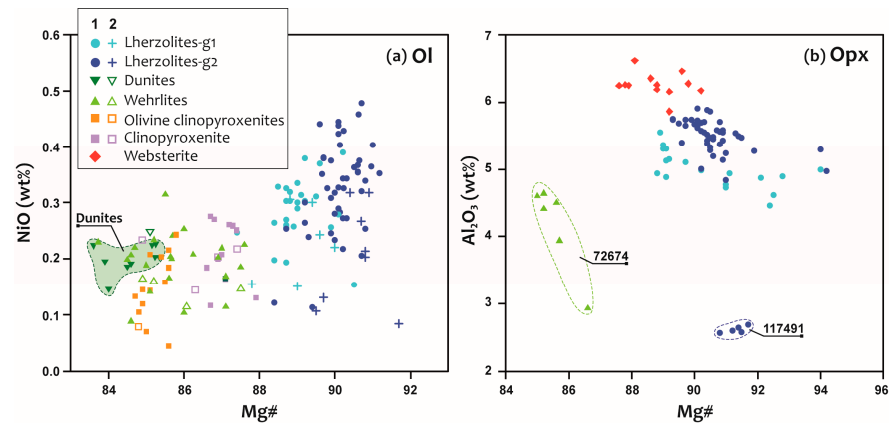


**Figure 8.** Major-element composition of olivine and orthopyroxene from the Cerro Pelado and El Palo peridotites and pyroxenite xenoliths. (a) NiO vs. Mg# in olivines; (b) Al<sub>2</sub>O<sub>3</sub> vs. Mg# in orthopyroxenes. Filled symbols represent primary mafic minerals (1), whereas empty ones are secondary neoblasts (2) in reaction zones. Mg# = [Mg/(Mg + Fe<sup>2+</sup>)] × 100, in mol.

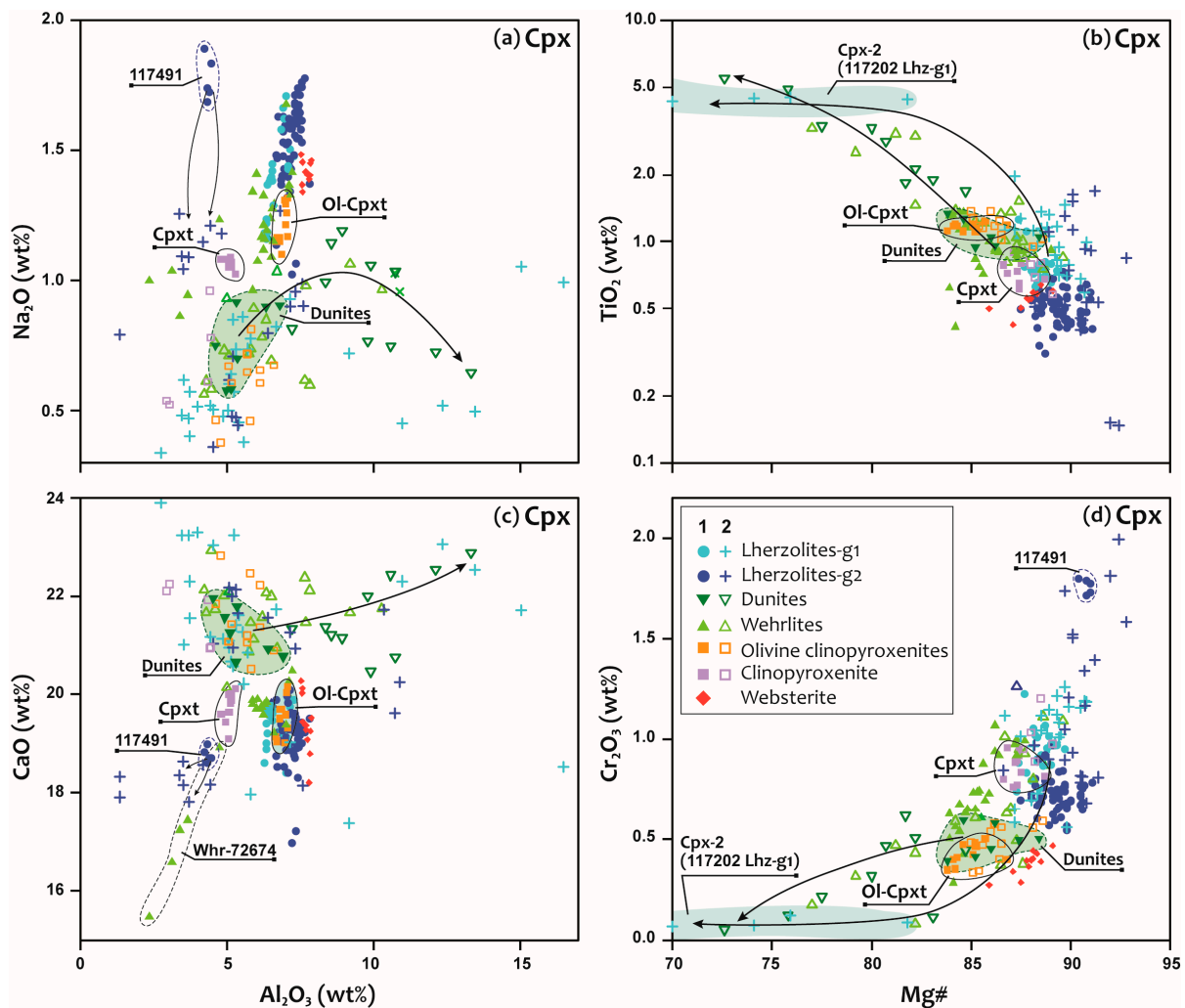


**Figure 9.** Major-element composition of clinopyroxene from the Cerro Pelado and El Palo ultramafic xenoliths. (a) Al<sub>2</sub>O<sub>3</sub> vs. Na<sub>2</sub>O; (b) Mg# vs. TiO<sub>2</sub>; (c) Al<sub>2</sub>O<sub>3</sub> vs. CaO; (d) Mg# vs. Cr<sub>2</sub>O<sub>3</sub>. Arrows show the broad chemical variation from primary crystals (1; filled symbols) to secondary neoblasts (2; empty symbols) in reaction zones. Ol-Cpxt = olivine clinopyroxenite, Cpxt = clinopyroxenite s.s., Lhz = lherzolite, Whr = wehrlite.

Clinopyroxene from clinopyroxenitic xenoliths shows similar compositional trends to those shown by the wehrlites, with a higher  $\text{TiO}_2$  content and lower Mg# and  $\text{Na}_2\text{O}$  than in lherzolites (Figure 9a,b,d). Clinopyroxene in olivine clinopyroxenites has a higher  $\text{Al}_2\text{O}_3$  and  $\text{TiO}_2$  and a lower  $\text{Cr}_2\text{O}_3$  content than in clinopyroxenites s.s. (Figure 9). Moreover, the websterite clinopyroxene generally shows a composition that is similar to the lherzolites, except for its slightly lower Mg# and  $\text{Cr}_2\text{O}_3$  contents (Figure 9).

Secondary clinopyroxene shows very wide compositional ranges, but the common feature in most of them is the increase in the  $\text{TiO}_2$  content compared to that of the primary one (Figure 9b). In the spongy and neoblastic clinopyroxene from the wehrlites and dunites, this Ti increase is accompanied by a Mg# decrease (Figure 9b). The most evolved composition is shown by elongated clinopyroxene neoblasts included in the glassy area from the lherzolite-g1 117202 (Figure 4b), which has the highest Ti-Fe enrichment of the main mafic minerals. These clinopyroxene-2 neoblasts, together with those from the dunites, also have higher  $\text{Al}_2\text{O}_3$  and CaO and lower  $\text{Cr}_2\text{O}_3$  contents than those of the primary ones (Figure 9 and Table S4). Secondary clinopyroxene from the lherzolite-g2 117491 has lower  $\text{Na}_2\text{O}$  and CaO contents than its corresponding primary clinopyroxene (Figure 9a,c). It should be noted that clinopyroxene-2 of lherzolites-g1 has a composition close to the apparently primary crystals from wehrlites and dunites, except for its MgO and  $\text{Cr}_2\text{O}_3$  contents, which are notably higher in these lherzolite neoblasts (Figure 9).

Primary spinel only occurs in lherzolites, showing considerable compositional differences. Spinel from lherzolites-g1 shows higher Cr# and  $\text{TiO}_2$  and correlatively lower Mg# contents than those of lherzolites-g2, except for spinel from the lherzolite-g2 117491, which is highlighted for its high Cr# and  $\text{TiO}_2$  contents (Figure 10a and Table S4). Spinel of the websterite shows very high  $\text{Al}_2\text{O}_3$  (up to 62 wt%) and low  $\text{Cr}_2\text{O}_3$  (3.6–5.8 wt%) contents compared to all other ultramafic xenoliths from the CVF [8–10] or from other volcanic fields [32,36]. Its  $\text{TiO}_2$  content is similar to the spinel from the lherzolites-g2 (Figure 10a).

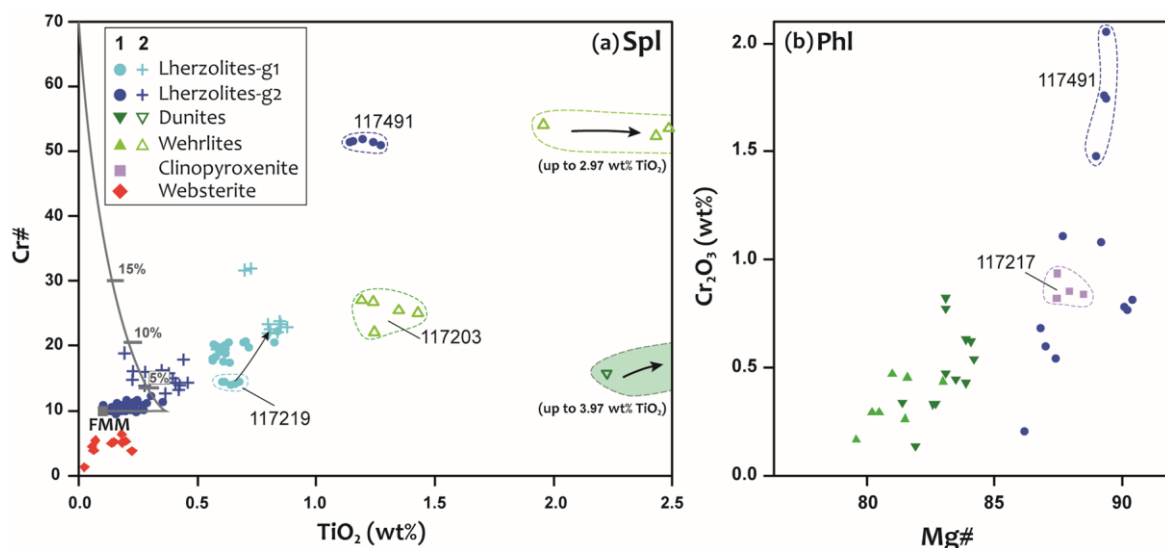


**Figure 10.** Major-element composition of spinel and phlogopite from the Cerro Pelado and El Palo ultramafic xenoliths. (a)  $\text{TiO}_2$  vs. Cr# in spinel; (b) Mg# vs.  $\text{Cr}_2\text{O}_3$  in phlogopite. Filled symbols are primary mafic mineral (1), and empty ones are secondary neoblasts (2) in reaction zones. Secondary spinel from wehrlite and dunite plots are outside of the diagram (a).  $\text{Mg\#} = [\text{Mg}/(\text{Mg} + \text{Fe}^{2+})] \times 100$ , in mol.  $\text{Cr\#} = [\text{Cr}/(\text{Cr} + \text{Al})] \times 100$ , in mol. FMM (Fertile MORB Mantle), according to [37].

Secondary spinel from lherzolites has lower  $\text{Al}_2\text{O}_3$  and Mg# contents and a higher Cr# content than those of the primary ones, with a correlative increase in  $\text{TiO}_2$  (Figure 10a). The compositional field of spinel from wehrlites and dunites are aligned with secondary-spinel

trends of lherzolites (e.g., a  $\text{Al}_2\text{O}_3$  decrease and  $\text{Cr}_2\text{O}_3$  and  $\text{TiO}_2$  enrichment, Figure 10a), suggesting its recrystallized origin.

Phlogopite from wehrlites and dunites has a lower Mg# content than that of lherzolites (Figure 10b), which is correlated with the increase in  $\text{TiO}_2$  and the decrease in  $\text{Cr}_2\text{O}_3$  and  $\text{Al}_2\text{O}_3$  contents (Figure 10b and Table S4). Phlogopite from the lherzolite 117491 is notably enriched in  $\text{TiO}_2$  and  $\text{Cr}_2\text{O}_3$  (Figure 10b and Table S4). Finally, small phlogopite crystals of the clinopyroxenite 117217 define a compositional field within common lherzolites (Figure 10b).

Amphibole from the lherzolite 111645 has the highest  $\text{K}_2\text{O}$  and  $\text{TiO}_2$  contents of all the metasomatic amphiboles found in the peridotite xenolith suites of the CVF (Supplementary Figure S1 and Table S4). Moreover, its chemical composition is very close to that of the associated amphibole megacrysts found in the Cerro Pelado volcano [27].

Interstitial glasses from wehrlites, lherzolites-g2, and most of the lherzolites-g1 have an alkaline composition, except for that closely related to the spongy clinopyroxene from the lherzolite-g1 117202, which shows a subalkaline composition between the trachyandesite and andesite types (Figure 11). Glasses of wehrlite 72674 and lherzolite-g2 65290 mostly overlap within the tephriphonolite and trachyandesite fields, whereas glass from lherzolite-g1 117202 is located close to the fields of xenolith groups 2 and 3 of the El Aprisco volcano [3] (Figure 11). Interstitial glass from the olivine clinopyroxenite 117480 highlights for having a marked subalkaline composition that is very far from the compositional fields of the other glasses of xenoliths from these volcanos (Figure 11). Finally, the compositional range of glasses from these xenoliths are markedly different from the field of the CVF magmatism.

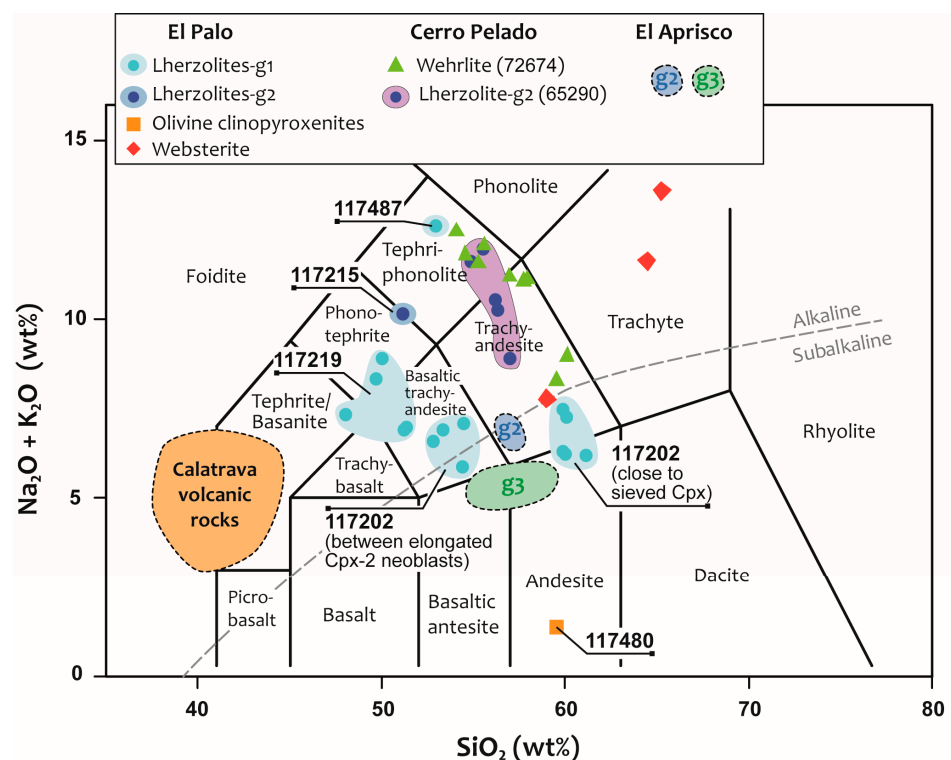


**Figure 11.** Glass composition of the Cerro Pelado and El Palo peridotite and pyroxenite xenoliths plotted in the total alkali-silica (TAS) diagram of [38]. Orange field is the compositional field of the Calatrava volcanic rocks [3], whereas g2 and g3 fields are glasses from the El Aprisco peridotite xenoliths taken from [4].

#### 4.3.2. Trace-Element Mineral Composition

Trace-element analyses of the rock-forming minerals of ultramafic xenoliths from the Cerro Pelado and El Palo volcanoes are reported in Supplementary Table S5. In chondrite-normalized REE diagrams, the primary clinopyroxenes from lherzolite groups

show LREE-rich patterns (Figure 12a), although those from lherzolites-g1 are more convex in LREE and are more fractionated than most of lherzolites-g2. In primitive mantle (PM)-normalized multi-trace diagrams, the primary clinopyroxene of both lherzolite groups displays similar patterns, with K-, Pb-, P-, Zr-Hf-, and Ti-negative and Th-U- and Ta-positive anomalies, except for the clinopyroxene from the lherzolite-g2 117491 which has a Zr-Hf-positive anomaly and Th-U values below the primitive mantle (Figure 12b).

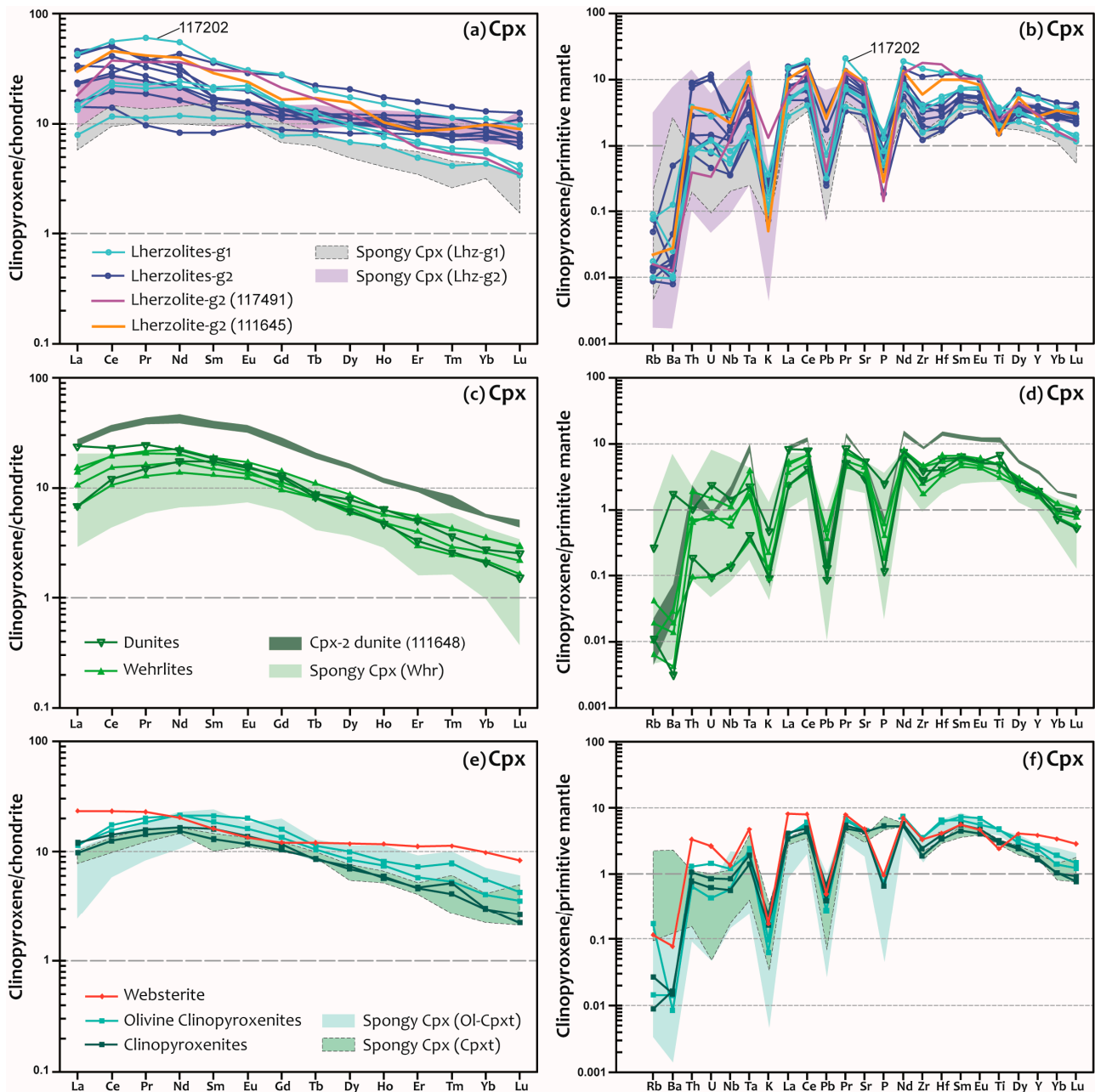


**Figure 12.** (a,c,e) Chondrite-normalized REE and (b,d,f) primordial mantle-normalized trace-element diagrams for averaged values of clinopyroxene from the Cerro Pelado and El Palo ultramafic xenoliths. Normalizing values are from [31].

The apparently primary clinopyroxenes from wehrlites and dunites show REE patterns that are similar to those of the clinopyroxenes from the lherzolites, although they have a lower REE content, especially in their LREE, having more convex profiles (Figure 12a,c). Furthermore, their Th-U contents are lower than those of most lherzolites, showing a small Ti-positive anomaly (Figure 12d). On the other hand, secondary clinopyroxene in the dunite

111648 shows a convex REE pattern, strongly fractionated in HREE that is parallel to that of the corresponding primary one but with higher values (Figure 12c). Its multi-trace diagram also shows a Ti-positive anomaly ( $10 \times$  primitive mantle values) (Figure 12d).

Clinopyroxene in clinopyroxenite xenoliths shows a similar trace-element composition in the two types, showing convex (MREE enrichment) and fractionated REE patterns (Figure 12e). However, clinopyroxene from olivine clinopyroxenites has a slightly higher REE and moderate incompatible-element (e.g., Zr, Hf, and Ti) contents than those of clinopyroxenites s.s. (Figure 12e,f). Clinopyroxene from the websterite shows a different REE composition compared to the other ultramafic xenoliths, with higher LREE and HREE contents, little fractionation (an almost flat pattern), and a slight concavity in the MREE (Figure 12e). Its multi-trace diagram has a similar pattern to clinopyroxenes of clinopyroxenites, although it has a slight Ti-negative anomaly (Figure 12f).

Spongy clinopyroxenes has lower REE and Th-U contents than those of apparently primary ones, but in wehrlites, their patterns are practically parallel to those of the corresponding primary clinopyroxene. Moreover, their Pb and P contents are similar to or lower than those of the accompanying primary clinopyroxene (Figure 12).

Orthopyroxene has trace-element contents that are markedly lower than the clinopyroxene. Their REE patterns are similar for the three types of xenoliths where they are found, showing a positive slope with a minor La-negative anomaly (Supplementary Figure S2a). The scarce orthopyroxene in the wehrlite 72674 has lower HREE and higher MREE, Hf, and Ti contents than those in lherzolites (Supplementary Figure S2a,b). In addition, orthopyroxene from lherzolites-g1 also has lower HREE and higher Zr-Hf and Ti contents than from lherzolites-g2 (Supplementary Figure S2a,b). Orthopyroxene from the El Palo websterite has similar REE and multi-trace-element patterns than those from other peridotite xenoliths (Supplementary Figure S2a).

Phlogopite from studied xenoliths has very low ( $<1 \times$  chondrite values) contents in most REE-Y, except for the strong positive anomaly in Eu-Gd (Supplementary Figure S2c). In multi-trace diagram, phlogopite shows positive LILE (K, Rb, and Ba), Nb-Ta, Pb, Sr, and Ti anomalies (Supplementary Figure S2d and Table S5). Phlogopite from the lherzolite-g2 111645 stands out for having the highest LREE and HREE contents, without an Eu-Gd-positive anomaly (Figure S2c,d). The scarce metasomatic amphibole (lherzolite 111645) shows a typical LREE convex pattern that is similar to that which is described to be associated with clinopyroxene, but its multi-trace pattern contrasts, showing a high positive Nb-Ta-K and Ti anomaly and a marked Th-U negative anomaly (Supplementary Figure S2e,f). It is worth noting that this multi-trace pattern is very similar to that found in amphibole megacrysts from this Cerro Pelado volcano [28] (Supplementary Figure S2f).

## 5. Discussion

### 5.1. Nature of the Mantle Sources

The peridotite xenoliths from the Cerro Pelado and El Palo volcanoes display much evidence of interactions with metasomatic agents. Thus, in order to characterize the most primitive lithospheric mantle protoliths, only the less-refertilized lherzolites (lherzolites-g2) were considered. To estimate the partial-melting degree of this mantle source, the variation in the clinopyroxene trace-element contents was used to obtain a more reliable calculation, as it is the main mineral that hosts the greatest HREE-Y amount in spinel peridotites [39]. Therefore, primary clinopyroxene from the lherzolites-g2 indicates that the most primitive peridotites from the Cerro Pelado and El Palo volcanoes would have undergone a low degree of partial melting ( $\leq 5\%$ ) (Supplementary Figure S3), which is similar to that obtained in other poorly metasomatized peridotite suites from the CVF [9,10].

This low partial-melting degree obtained in most of the primitive CVF lherzolites contrasts with values estimated in other peridotite xenolith suites from the Cenozoic volcanic fields of Iberia. Thus, in the Olot area, the lherzolite xenoliths yield modelled melting fractions of up to 7% and even higher when harzburgite types (up to 30%–40%) are involved [32,40]. Moreover, the presence of harzburgite and orthopyroxene-rich lherzolite

xenoliths in the Tallante volcanic area (SE Spain) also suggests large partial-melting degrees for its sampled lithospheric mantle xenolith suite, in agreement with the high Cr# values of associated spinels [41–43]. The low Cr, Ni, and Mg contents of the mafic minerals of the Cerro Pelado and El Palo mantle xenoliths are also indicative of a more fertile character of the lithospheric mantle beneath Central Spain when compared to the mantle xenolith suites of the rest of the alkaline Iberian volcanic fields.

Nevertheless, the whole-rock and apparent primary clinopyroxenes of studied lherzolites from the Cerro Pelado and El Palo volcanoes show marked LREE-rich patterns (Figures 6a and 12a). This contrasts with previous studies of CVF peridotite xenolith suites, indicating that the less-refertilized peridotites have an REE composition that is close to depleted-mantle component (N-MORB-like) patterns [9,10]. Therefore, the Cerro Pelado and El Palo lherzolites have subsequently undergone a certain degree of cryptic metasomatism, and their partial-melting modelling might be considered as approximate values.

Isotopic composition of studied ultramafic xenoliths plot in the compositional field of Calatrava volcanic rocks (Figure 7), indicating the close genetic relationship of their refertilization to the associated alkaline volcanism. Previous studies [44] suggested that Calatrava volcanic rocks constitute a set of magmas with variable and small partial-melting degrees (5%–17%) of a mantle source enriched with phlogopites (and amphibole) and with values of incompatible elements from 1.2 to 10× the primitive-mantle values. Although the here-studied peridotite xenoliths appear to be derived from mantle protoliths with low partial-melting degrees, the HREE-depleted character of most of the Calatrava volcanic rocks are indicative of a deeper mantle source than those peridotite xenoliths (spinel facies lithospheric mantle) within the garnet stability field and that are already in the asthenosphere.

## 5.2. Nature of Metasomatic Events in Peridotite Xenoliths

### 5.2.1. Origin of Cryptically Metasomatized Lherzolites and Fe-Ti-Rich Wehrlites

Cryptic metasomatism occurs in all ultramafic xenoliths from the two studied volcanic centers, whereas only some peridotites show modal metasomatism (i.e., occurrence of phlogopites and amphiboles), mainly in the more evolved varieties of the Cerro Pelado (wehrlites and dunites, Table 1).

The REE and multi-trace patterns of most of the studied peridotite xenoliths (Figure 6) are broadly similar. Therefore, spinel lherzolites, wehrlites, and dunites might have undergone a similar alkaline metasomatism but with slight differences in their intensity. All these rocks show LREE-enrichment with a convex shape in the REE-normalized diagrams of whole-rock composition (Figure 6a) and of the apparent *primary* clinopyroxene (Figure 12a,c), a marked HREE fractionation, and a lack of a Nb-Ta-negative anomaly in multi-trace clinopyroxene patterns (Figure 12b,d). Some features are progressively more marked from lherzolites-g1 to wehrlites, via lherzolites-g2: (1) lherzolitic clinopyroxenes have multi-trace patterns with a slight negative Ti anomaly, which lacks in most of clinopyroxene patterns from wehrlites and dunites (Figure 12b,d); (2) clinopyroxenes from lherzolites-g1 show more fractionated REE profiles than those of g2 type and a slightly less-pronounced negative Ti anomaly, approaching the patterns of metasomatic wehrlites and dunites (Figure 12a–d); (3) the convex shape of the LREE gradually increases from lherzolites-g1, -g2, wehrlites to dunites in the same way as the more fractionated HREE patterns (Figure 12a,c); and (4) the modal abundance of metasomatic minerals is higher in wehrlites and dunites (up by 7.9 modal%) than in lherzolites-g2 (0.1–0.9 modal%), being absent in lherzolites-g1.

The origin of wehrlites has been broadly discussed as accumulations of mantle-derived mafic melts or by peridotite–metasomatic reactions with alkaline carbonate-rich [45] or silica-undersaturated melts [12,46]. Several features point out that the studied wehrlites could be the result of the metasomatic transformation of a lherzolite protolith [3]. They do not show igneous textures typical of cumulates (e.g., mineral zoning), and olivine usually displays curvilinear shapes and deformation twins. In the wehrlite that preserves orthopyroxene crystals (Table 1), these have smaller sizes than those of the lherzolites, in addition

to corroded shapes (Figure 3c). The similar  $\text{Al}_2\text{O}_3$  content of this wehrlite orthopyroxene with that of lherzolites (Figure 8b) suggests an advanced state of orthopyroxene dissolution from a lherzolite protolith. In the rest of wehrlites and dunites, orthopyroxene does not appear, indicating a strong interaction with  $\text{SiO}_2$  undersaturated melts for a longer period of time [47]. Moreover, most of the studied wehrlite xenoliths show a marked enrichment in Fe-Ti and Ca and a depletion in the Ni content compared to lherzolite (Figure 5), which is typical of a silicate alkaline metasomatic agent for their origin, instead of a carbonate-rich melt [45,48]. These chemical changes are similar to those described for other Fe-Ti-rich lherzolite–wehrlite series formed by alkaline-melt percolation through associated lherzolites [12]. As shown in Figure 13, wehrlite (and dunite) clinopyroxenes plot in the compositional fields of refertilization by silicate alkaline melts. This contrasts with wehrlite xenoliths from the CVF's El Aprisco maar, which were metasomatized by carbonatite melts [4,7].

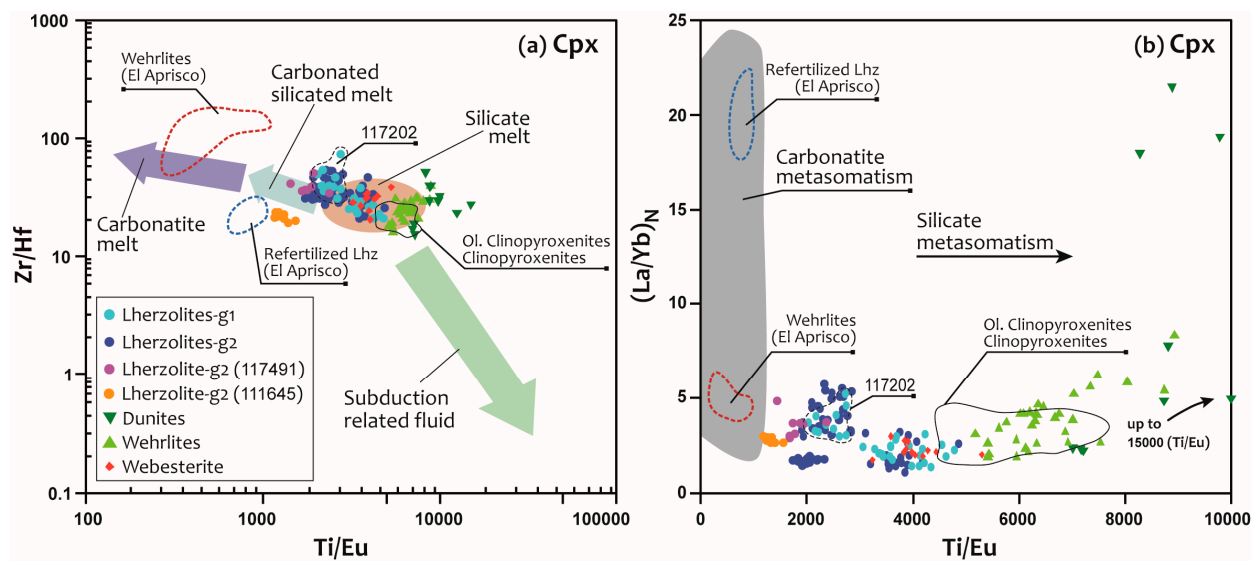


**Figure 13.** Clinopyroxene trace-element composition of the Cerro Pelado and El Palo ultramafic xenoliths groups. (a) Ti/Eu vs. Zr/Hf ratios with trends for different metasomatizing agents from [49]; (b) Ti/Eu vs. La/Yb chondrite-normalized (N) ratios and fields for carbonatite (shaded area) and silicate melt metasomatism are adapted from [45]. Clinopyroxene from wehrlites and lherzolites metasomatized by carbonatite melts from the El Aprisco volcano (red and blue compositional fields) [7] have been included for comparison.

Clinopyroxene from lherzolites has lower Ti/Eu ratios than those of dunites and wehrlites, suggesting an interaction with slightly carbonated melts (Figure 13). Nevertheless, clinopyroxene of some lherzolites, having the lowest Ti/Eu ratios, lacks negative Zr-Hf anomalies (Figures 12 and 13), clearly ruling out the possibility of a carbonatitic metasomatic agent. Chemical composition of metasomatic agents can also be obtained by calculating the theoretical liquids in equilibrium with the cryptically metasomatized clinopyroxene, using partition coefficients from basaltic systems [50–52]. The estimated melt compositions in equilibrium with clinopyroxene from wehrlites, dunites, and lherzolites from the Cerro Pelado and El Palo show similar REE and multi-trace patterns, which, in turn, are similar to the composition of the Calatrava volcanic rocks (Figure 14). These calculated melts show positive Nb-Ta anomalies and a very small (or no) Zr-Ti negative anomalies, ruling out the interaction with carbonatitic melts [53], unless a later more silica-rich alkaline metasomatism superimposed the carbonatitic one. In addition, the similar REE and multi-trace patterns of the metasomatic amphibole and cryptically metasomatized clinopyroxene and those shown by megacrysts from the Cerro Pelado volcano (Figure 14 and Supplementary Figure S2e,f) reinforce the idea that the alkaline CVF magmatism might be the main source of the refertilization shown by the studied xenolith suite.

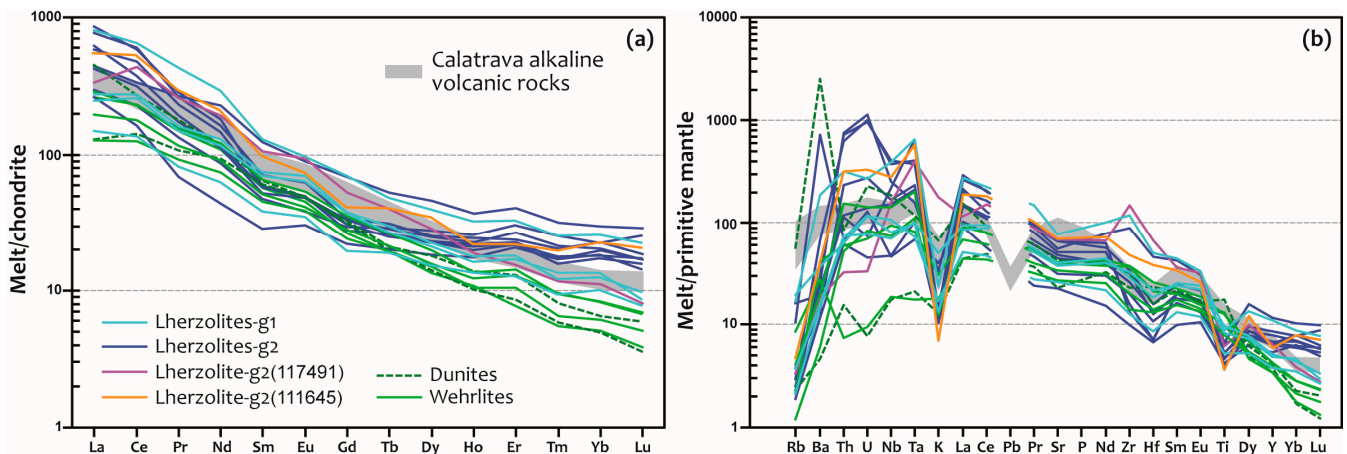


**Figure 14.** Calculated melts in equilibrium with averaged clinopyroxene from the Cerro Pelado and El Palo peridotites. (a) Chondrite-normalized REE; and (b) primordial mantle normalized trace-element patterns. Calatrava alkaline volcanic rocks [34,44] are also included for comparison. Melt compositions were calculated using cpx-basaltic melt partition coefficients [50,52], except for Rb [51]. Normalizing values for chondrite and primitive mantle are from [31].

### 5.2.2. Origin of Pyroxenite Xenoliths

Pyroxenitic xenoliths are common in kimberlites and alkaline basalts, and their origin remains highly debated: (i) they can be formed by intense metasomatism induced by melt-peridotite reactions; (ii) or they can be the product of mafic magmatism crystallizing at the crust–mantle boundary [54–59]. The pyroxenitic xenoliths from the El Palo volcano (clinopyroxenites and websterite, Table 1) are texturally very different to the magmatic clinopyroxenite cumulates that have been identified as autoliths in other CVF volcanoes, linked to the Calatrava magmatism [27]. Moreover, the formation of studied pyroxenites at depths close to the crust–mantle boundary and the presence of pyroxenite granulites in the lower crust of Central Iberia [60] could suggest an origin by accumulation of mafic magmas in the shallowest lithospheric mantle. However, the El Palo pyroxenites lack negative Eu anomalies and present a higher degree of HREE fractionation (Figure 6c,d) than granulitic xenoliths from alkaline lamprophyres of Central Iberia [60]. In the case of the El Palo websterite, its orthopyroxene also lacks an Eu anomaly and shows a higher Mg and Cr and a lower Ti and Fe content than orthopyroxene from a granulitic websterite xenolith from Central Iberia. Nevertheless, similar REE compositions of studied clinopyroxenitic xenoliths and pyroxenite cumulates of the Calatrava magmas [28] may be a consequence of the common alkaline nature between the metasomatic agent that has transformed these mantle xenoliths and the own Calatrava magmatism. However, the high  $\text{Al}_2\text{O}_3$  content of the websterite orthopyroxene (Figure 8b) suggests different alkaline metasomatic conditions (higher pressure of equilibration) than those for associated clinopyroxenites, which is in agreement with melt infiltration experiments of [29].

Sr–Nd isotopic data of studied lherzolite, wehrlite, and pyroxenite xenoliths overlap in a field comprising the HIMU-FOZO-EAR compositions and coincide with the data of the Calatrava volcanism (Figure 7), again suggesting a similar source for alkaline metasomatic agents that interacted with these peridotites and pyroxenites. The MORB-type eclogitic nature of this FOZO-HIMU component, as suggested by [2], is neither corroborated by our isotopic data nor by the high  $\text{TiO}_2/\text{FeO}$  ratios of the studied pyroxenite xenoliths.

### 5.3. Origin of the Interstitial Glass

Glass in these xenoliths appears mainly in disconnected melt pockets or veinlets of a limited trail (Figure 4b,f), which frequently contains neo-formed clinopyroxene, olivine, and spinel microcrystals (Figure 4f). Indeed, they have vesicles or vacuoles (empty voids of Figure 4b,d,f), suggesting volatile exsolution by decompression during volcanic transport to

the surface. The interstitial glass composition from the Cerro Pelado and El Palo ultramafic xenoliths is very different from the CVF magmas (Figure 11), in principle ruling out an origin by infiltration of the volcanic magma that transported the xenoliths.

Glasses from some of the Cerro Pelado and El Palo peridotites show a great similarity in chemical composition with experimental studies on melting peridotites, which usually yield trachyandesitic glass compositions [61,62] (Figure 11). The high  $\text{TiO}_2 + \text{K}_2\text{O}$  contents (in the range of 5.3–7.2) of these glasses are in agreement with an alkaline metasomatism of the original lherzolite, previously to this limited partial-melting process. Moreover, studied glass-compositional variability is explained by the peridotite composition, the variable mineral proportions in the local partial-melting reactions, and also by the consequent crystallization of secondary minerals (Cpx-2, Ol-2, and Spl-2) in different amounts.

The partial-melting reaction would be favored by the breakdown of hydrated metasomatic minerals (amphibole and phlogopite) during the xenolith rise within the volcanic magma, producing small melt fractions [63–65]. However, the Cerro Pelado and El Palo xenoliths show neither significant amounts of hydrated metasomatic minerals nor clear petrographic indications of their involvement. Although the studied peridotites can be considered mainly anhydrous, they may have undergone partial melting during their trapping (thermal input) and quick volcanic transport, especially if they were previously refertilized. The metasomatic character of these ultramafic rocks (clinopyroxene-rich) might have substantially modified their solidus curves to a lower temperature than those of the non-metasomatized lherzolites [66], favoring the in situ partial melting of these centimeter-sized xenoliths. Adiabatic decompression during their transport through the upper lithosphere (probably lasting a few tens of hours, since they are trapped, according to [5]) would facilitate low degrees of partial melting of the xenolith.

In studied lherzolites, wehrlites, and clinopyroxenites s.l., glass also appears as inclusions in the spongy clinopyroxene. Previous studies [67,68] propose that the spongy texture and associated glass originate during decompression in anhydrous xenoliths (without modal hydrated metasomatic minerals). Accordingly, linked to partial melting in spinel lherzolites, different spongy textures also originate around the spinel (Figure 4b,d). All these textures would be produced by incongruent dissolution followed by nucleation and a subsequent quick growth of the new mineral neoblasts within the crystal-interstitial melt area [69]. The higher  $\text{TiO}_2$  and  $\text{Cr}_2\text{O}_3$  contents of secondary spinel contrast with those of the primary one (Figure 10a), in agreement with in situ melting processes [70]. The acicular morphology of clinopyroxene crystals within glass domains (Figure 4b,d) also indicates a metastable rapid crystallization.

The most-evolved ultramafic xenoliths (wehrlites and pyroxenites) usually present interstitial glasses (Table 1). In these xenoliths, glass also occurs in disconnected melt pockets with abundant vesicles or as irregular nano-pockets within the spongy texture of clinopyroxenes (Figure 4b,d). These textural features also indicate variable partial-melting degrees during the xenolith reheating and depressurization, which is linked to its incorporation into a high-temperature basaltic melt and its rapid and adiabatic transport to the surface.

The wehrlite 72674 from the Cerro Pelado has tephriphonolite and trachyandesite glass compositions, while trachyte-trachyandesite (websterite) or andesite (olivine clinopyroxenite) are from developed pyroxenites (Figure 11), which are glasses that are more felsic in composition than those generated from lherzolites and are sometimes even subalkaline (andesitic glass from olivine clinopyroxenite 117480, Figure 11). It is also worth noting their enrichment in  $\text{K}_2\text{O}$ , which, on many occasions, is similar or even higher than the  $\text{Na}_2\text{O}$  content (Supplementary Table S4), pointing to a near-shoshonitic composition. K-rich interstitial glasses have also been described in refertilized peridotite xenoliths from other volcanic areas, which are also linked to in situ partial melting during their transport to the surface [70]. In our case, the occurrence of phlogopites, exclusive to these xenoliths of the CVF, might be related to these compositional features.

#### 5.4. Calatrava Subcontinental Lithospheric Mantle

Although a large part of the SCLM sampled by volcanic magmas of the CVF shows evidence of having undergone strong alkaline refertilization, some mantle xenoliths without significant metasomatism have also been sampled [9,10]. These lherzolite xenoliths can be considered an inherited domain of a pristine lithospheric mantle with REE patterns close to a depleted-mantle composition, the main source of the MORB-type magmas (M1; Figure 15). They show isotopic compositions far from the EAR-HIMU components, defining a broad mixing band between the MORB compositional fields and an enriched EMII component in the Sr–Nd isotopic plot (Figure 7). The studied ultramafic xenoliths of the Cerro Pelado and El Palo are compositionally out from that array.

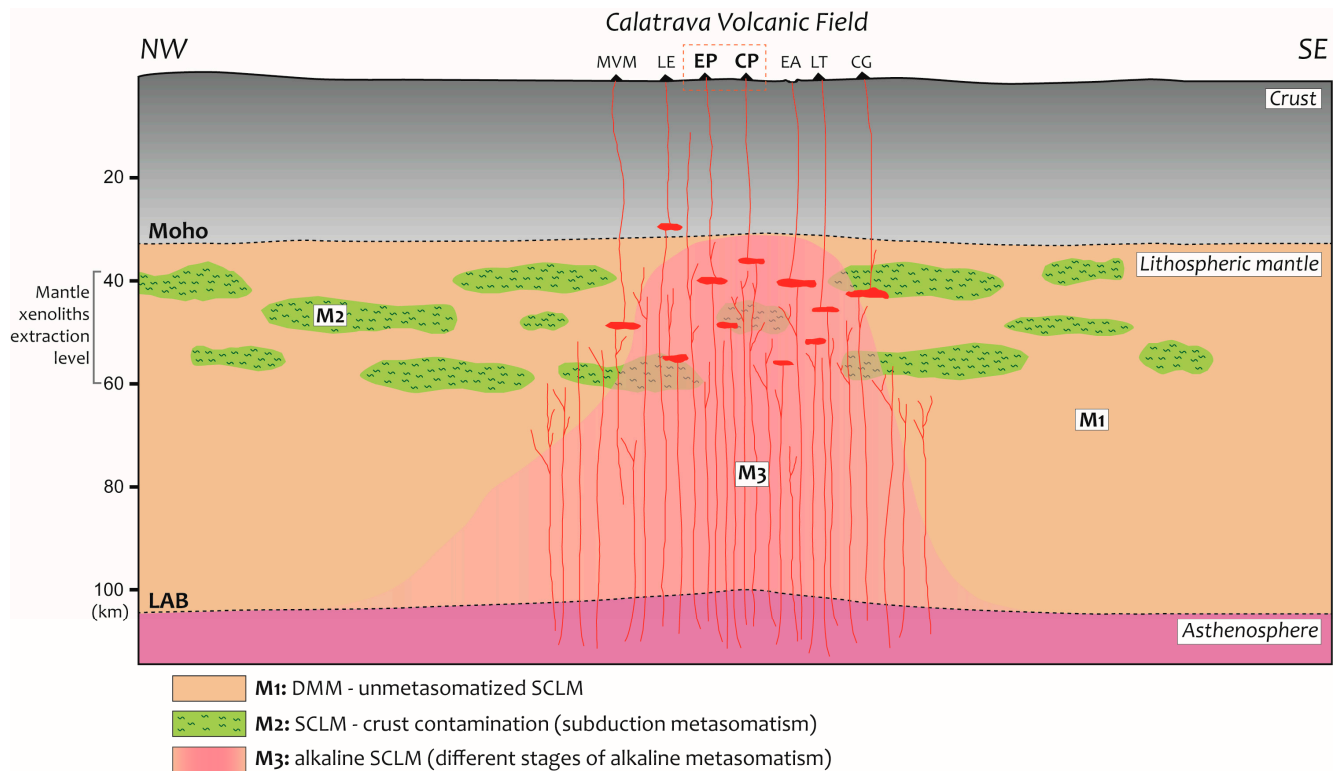


**Figure 15.** Interpretative section of the different types of SCLMs sampled by the CVF volcanoes (modified from [8]). The three upper lithospheric mantle types, sampled by the Calatrava magmatism, are as follows: **M1**: an unrefertilized SCLM with a DMM component (depleted MORB mantle) [9,10]. **M2**: an SCLM with a cortical component, refertilized by subduction metasomatism [10] and supposedly due to a delamination of the lower crust into the SCLM during the Variscan period. **M3**: alkaline SCLM generated during several refertilization stages by alkaline melts from the Cretaceous up to the Cenozoic Calatrava magmatism [7]. Volcanoes: MVM = Morrón de Villamayor, LE = La Encomienda, EP = El Palo, CP = Cerro Pelado, EA = El Aprisco, LT = Los Tormos, CG = Cerro Gordo.

Ultramafic xenolith suites from the Cerro Gordo volcano define a second mantle domain of this Iberian SCLM affected by metasomatic subduction agents, which is probably linked to the Variscan continental collision [10]. In this sector, this collision was intracontinental in nature and might have generated delamination and subsidence of the lower crust into the subcontinental lithospheric mantle [34]. The infiltration of magmas derived from this mantle that was contaminated by cortical fragments would have refertilized the upper lithospheric mantle levels (M2; Figure 15), giving rise to LREE-LILE-Th-U-Pb-rich lherzolites with marked Nb-Ta-negative anomalies, as occurs in some mantle xenoliths sampled from the El Aprisco and Cerro Gordo volcanoes [4,10].

Nevertheless, most lithospheric mantle xenoliths of the CVF (as in the here-studied Cerro Pelado and El Palo) show metasomatism and a marked refertilization by an interac-

tion with successive alkaline melts during at least four magmatic events arising from the Cretaceous to Pleistocene times [7]. This succession of alkaline magmatism also defines a temporal chemical evolution from Cretaceous and Oligocene carbonatitic to Miocene and Pliocene silica-undersaturated imprints of the alkaline metasomatism of these lithospheric peridotite suites [7].

In the western Circum-Mediterranean Anorogenic Cenozoic Igneous Province [CiMACI; 17], some studies have attempted to discriminate the broad spectra of SCLM types. In this way, some authors [71], for Alpine areas, proposed a hypothesis of mantle variability during a Wilson cycle, showing some coherent compositional trends in time and space, differentiating three main domains: (i) an inherited domain; (ii) a refertilized domain; and (iii) an oceanic depleted domain related to Alpine seafloor spreading.

In the CVF, there are two different inherited mantle domains, and the oldest may be a DMM that was probably formed during seafloor and oceanic subduction in mantle wedges of arc settings when the peri-Gondwanan Iberian microplate occupied a Cadomian margin [10,34]. The second inherited SCLM component is the Variscan orogenic mantle that is common in many other European Cenozoic volcanic fields (e.g., Silesia [72] and the French Massif Central [33,49]). The coincidence in Re-Os model ages from some CVF mantle xenoliths with the Cadomian and Variscan orogenic times reinforce the idea of a substantial crustal–mantle interaction at those periods in Central Iberia [73]. Finally, the refertilized SCLM domain is dominant in the CiMACI, as successive inputs of Cenozoic alkaline magmatism widely overprinted the shallow mantle lithosphere levels in all the CiMACI, from where the xenoliths were extracted [72], as described in the here-studied Cerro Pelado and El Palo xenolith suites.

## 6. Conclusions

The peridotite and pyroxenite xenoliths from the Cerro Pelado and El Palo volcanic centers have allowed for several inferences regarding the lithospheric mantle beneath the CVF:

- (1) Four groups of ultramafic xenoliths have been distinguished in the Cerro Pelado and El Palo volcanic centers according to petrographic and compositional features: lherzolites, wehrlites-dunites, clinopyroxenites, and websterites. All of them show evidence of alkaline metasomatism, although in a variable degree. Lherzolites represent the less-refertilized mantle composition, whereas the other xenoliths would define trends of a more intensive transformation by silicate alkaline melts.
- (2) In situ partial melting during volcanic transport of the xenolith is considered the origin of the interstitial glass in the here-studied CVF peridotites. In the case of those anhydrous xenoliths (showing cryptic metasomatism, mainly in its clinopyroxene), partial melting would have been favored by their lower solidus temperature than for lherzolites and triggered by the thermal input and adiabatic decompression during their travel to the surface within the volcanic magma.
- (3) Most of the studied xenolith samples define a common trend of Fe-Ti-Ca enrichment in comparison with other CVF xenolith suites, although pyroxenites are depleted in Fe compared to associated lherzolites and wehrlites. Trace-element patterns are roughly similar, suggesting different conditions and refertilization degrees by alkaline silicate melts. In wehrlites, dunites, and clinopyroxenites, this refertilization has almost completely consumed all the primary orthopyroxene.
- (4) The singular El Palo websterite xenolith might represent a variety of alkaline metasomatism formed in a broad reaction zone with high melt–peridotite interaction rates occurring at higher pressure conditions than associated wehrlites or clinopyroxenites. This is markedly dissimilar to websterite enclaves (granulites) from the Spanish Central System, which have been interpreted as magmatic cumulates.
- (5) The here-studied Cerro Pelado and El Palo ultramafic xenoliths have an alkaline imprint, the most common refertilization in alkaline intraplate European Cenozoic volcanic fields. Alkaline magmatism in Iberia might be linked to extension processes

from the Mesozoic to the Cenozoic periods. The great similitude with the Sr–Nd isotopic EAR–HIMU composition, along with metasomatic clinopyroxene (and amphibole) trace-element patterns being similar to those from megacryst-phenocrysts of Calatrava volcanics, highlights the main role of this last alkaline magmatism in metasomatic processes beneath Central Iberia. This alkaline-refertilized mantle adds to two other SCLM types described in Calatrava. The oldest one would correspond to a mantle domain close to a depleted-mantle (DMM) composition, whereas the second mantle type records metasomatic subduction imprints, which are probably linked to the Variscan collision.

**Supplementary Materials:** The following supporting information can be downloaded at: <https://www.mdpi.com/article/10.3390/min14030241/s1>, Figure S1: Mg# vs. K<sub>2</sub>O of amphibole from lherzolite-g2 111645 from the Cerro Pelado volcano. Figure S2: Chondrite-normalized REE and primordial mantle-normalized trace element diagrams for averaged values of orthopyroxene, phlogopite and amphibole from the Cerro Pelado and El Palo xenoliths. Figure S3: Partial melting results for Y and Yb in clinopyroxene from the Cerro Pelado and El Palo lherzolites-g2. Table S1: Reference materials used in LA-ICPMS analyses. Table S2: Whole-rock (major and trace elements) analyses. Table S3: Whole-rock Sr–Nd isotope data. Table S4: Mineral chemistry (major elements). Table S5: Mineral chemistry (trace elements).

**Author Contributions:** Conceptualization and investigation: J.G.S., C.V. and C.P.-S.; Methodology and analytical data: J.G.S. and M.J.R.-A.; Writing original draft: J.G.S. and C.V.; Writing, review and editing: J.G.S., C.V., C.P.-S. and M.J.R.-A.; Supervision: C.V. and C.P.-S.; Funding acquisition: C.V. All authors have read and agreed to the published version of the manuscript.

**Funding:** This work is supported by a project of the Ministerio de Ciencia e Innovación (MICIN) of Spain (PID2020-115980GB-I00).

**Data Availability Statement:** Data are contained within the article and Supplementary Materials.

**Acknowledgments:** The authors wish to thank Alfredo Fernández Larios for helping in the mineral chemical analyses by electron microprobe (Centro Nacional de Microscopía Electrónica, UCM) and José Manuel Fuenlabrada for helping with performing the Sr–Nd isotopic analyses (CAI de Geocronología y Geoquímica Isotópica, UCM). This paper was improved by critical comments and suggestions by four anonymous reviewers that also helped us in the correction of some minor typographic mistakes and grammatical errors in a previous version of the manuscript.

**Conflicts of Interest:** The authors declare no conflicts of interest.

## References

1. Downes, H. Formation and modification of the shallow sub-continental lithospheric mantle: A review of geochemical evidence from ultramafic xenoliths suites and tectonically emplaced ultramafic massifs of western and Central Europe. *J. Petrol.* **2001**, *42*, 233–250. [[CrossRef](#)]
2. Bianchini, G.; Beccaluva, L.; Bonadiman, C.; Nowell, G.M.; Pearson, D.G.; Siena, F.; Wilson, M. Mantle metasomatism by melts of HIMU piclogite components: New insights from Fe-lherzolite xenoliths (Calatrava Volcanic District, Central Spain). In *Petrological Evolution of the European Lithospheric Mantle*; Coltorti, M., Downes, H., Grégoire, M., O'Reilly, S.Y., Eds.; Special Publications 337; Geological Society: London, UK, 2010; pp. 107–124.
3. Villaseca, C.; Ancochea, E.; Orejana, D.; Jeffries, T.E. Composition and evolution of lithospheric mantle in Central Spain: Inferences from peridotite xenoliths from the Cenozoic Calatrava volcanic field. In *Petrological Evolution of the European Lithospheric Mantle*; Coltorti, M., Downes, H., Grégoire, M., O'Reilly, S.Y., Eds.; Special Publications 337; Geological Society: London, UK, 2010; pp. 125–151.
4. González-Jimenez, J.M.; Villaseca, C.; Griffin, W.L.; O'Reilly, S.Y.; Belousova, E.; Ancochea, E. Significance of ancient sulphide PGE and Re–Os signatures in the mantle beneath Calatrava, Central Spain. *Contrib. Mineral. Petrol.* **2014**, *168*, 1047. [[CrossRef](#)]
5. Lierenfeld, M.B.; Mattsson, H.B. Geochemistry and eruptive behaviour of the Finca la Nava maar volcano (Campo de Calatrava, south-central Spain). *Int. J. Earth Sci.* **2015**, *104*, 1795–1817. [[CrossRef](#)]
6. Puelles, P.; Ábalos, B.; Gil Ibarra, J.I.; Sarrionandia, F.; Carracedo, M.; Fernández-Armas, S. Petrofabric and seismic properties of lithospheric mantle xenoliths from the Calatrava volcanic field (Central Spain). *Tectonophysics* **2016**, *683*, 200–215. [[CrossRef](#)]
7. Villaseca, C.; Belousova, E.; Barfod, D.; González-Jiménez, J.M. Dating metasomatic events in the lithospheric mantle beneath the Calatrava volcanic field (Central Spain). *Lithosphere* **2019**, *11*, 192–208. [[CrossRef](#)]

8. García Serrano, J. Petrología y Geoquímica de los Xenolitos del Manto en los Volcanes del Campo de Calatrava (Ciudad Real, España). Ph.D. Thesis, Complutense University, Madrid, Spain, 2023; 299p.
9. García Serrano, J.; Villaseca, C.; Pérez-Soba, C. Depleted lherzolite xenoliths from the leucititic Morrón de Villamayor volcano (Calatrava volcanic field, Spain). *Lithos* **2021**, *380–381*, 105830. [[CrossRef](#)]
10. Villaseca, C.; García Serrano, J.; Pérez-Soba, C. Subduction-related metasomatism in the lithospheric mantle beneath the Calatrava volcanic field (central Spain): Constraints from lherzolite xenoliths of the Cerro Gordo volcano. *Int. Geol. Rev.* **2022**, *64*, 469–488. [[CrossRef](#)]
11. García Serrano, J.; Villaseca, C.; Pérez-Soba, C. Xenolitos peridotíticos y piroxeníticos del volcán El Palo (Campo Volcánico de Calatrava, España). *Geotemas* **2021**, *18*, 422–425.
12. Ionov, D.A.; Chanefo, I.; Bodinier, J.L. Origin of Fe-rich lherzolites and wehrlites from Tok, SE Siberia by reactive melt percolation in refractory mantle peridotites. *Contrib. Mineral. Petrol.* **2005**, *150*, 335–353. [[CrossRef](#)]
13. Ackerman, L.; Jelínek, E.; Medaris Jr, G.; Ježek, J.; Siebel, W.; Strnad, L. Geochemistry of Fe-rich peridotites and associated pyroxenites from Horní Bory, Bohemian Massif: Insights into subduction-related melt–rock reactions. *Chem. Geol.* **2009**, *259*, 152–167. [[CrossRef](#)]
14. Ancochea, E. Evolución Espacial y Temporal del Vulcanismo Reciente de España Central. Ph.D. Thesis, Complutense University, Madrid, Spain, 1982; 675p.
15. Cebriá, J.M.; Martín-Escorza, C.; López-Ruiz, J.; Morán-Zenteno, D.J.; Martiny, B.M. Numerical recognition of alignments in monogenetic volcanic areas: Examples from the Michoacán- Guanajuato Volcanic Field in Mexico and Calatrava in Spain. *J. Volcanol. Geotherm. Res.* **2011**, *201*, 73–82. [[CrossRef](#)]
16. Ancochea, E. Rasgos generales del vulcanismo Neógeno peninsular. In *Geología de España*; Vera, J.A., Ed.; SGE-IGME: Madrid, Spain, 2004; pp. 671–672.
17. Lustrino, M.; Wilson, M. The circum-Mediterranean anorogenic Cenozoic igneous province. *Earth Sci. Rev.* **2007**, *81*, 1–65. [[CrossRef](#)]
18. De Vicente, G.; Vegas, R. Large-scale distributed deformation controlled topography along the western Africa-Eurasia limit: Tectonic constraints. *Tectonophysics* **2009**, *474*, 124–143. [[CrossRef](#)]
19. López-Ruiz, J.L.; Cebriá, J.M.; Doblas, M. Cenozoic volcanism in the Iberian Peninsula. In *The Geology of Spain*; Gibbons, W., Moreno, T., Eds.; The Geological Society: London, UK, 2002; pp. 417–438.
20. López Ruiz, J.; Cebriá, J.M.; Doblas, M.; Oyarzun, M.; Hoyos, M.; Martín, C. The late Cenozoic alkaline volcanism of the Central Iberian Peninsula (Calatrava Volcanic Province, Spain): Intra-plate volcanism related to extensional tectonics. *J. Geol. Soc. Lond.* **1993**, *150*, 915–922. [[CrossRef](#)]
21. Ancochea, E.; Huertas, M.J. Radiometric ages and time-space distribution of volcanism in the Campo de Calatrava Volcanic Field (Iberian Peninsula). *J. Iber. Geol.* **2021**, *47*, 209–223. [[CrossRef](#)]
22. Carminati, E.; Lustrino, M.; Doglioni, C. Geodynamic evolution of the central and western Mediterranean: Tectonics vs. igneous petrology constraints. *Tectonophysics* **2012**, *579*, 173–192. [[CrossRef](#)]
23. Granja Bruña, J.L.; Vegas, R.; Sentre, M.A.; Muñoz-Martín, A.; Sainz-Maza, S. Gravity modeling of the lithosphere in the Calatrava Volcanic Province (Spain): Geodynamic implications. *J. Iber. Geol.* **2015**, *41*, 233–252. [[CrossRef](#)]
24. Paton, C.; Hellstrom, J.; Paul, B.; Woodhead, J.; Hergt, J. Iolite: Freeware for the visualisation and processing of mass spectrometric data. *J. Anal. At. Spectrom.* **2011**, *26*, 2508–2518. [[CrossRef](#)]
25. Woodhead, J.; Hellstrom, J.; Hergt, J.; Greig, A.; Maas, R. Isotopic and elemental imaging of geological materials by laser ablation Inductively Coupled Plasma mass spectrometry. *Geostand. Geoanal. Res.* **2007**, *31*, 331–343. [[CrossRef](#)]
26. Dahlquist, J.A.; Galindo, C.; Morales Camera, M.M.; Moreno, J.A.; Alasino, P.H.; Basei, M.A.S.; Macchioli Grande, M. A combined zircon Hf isotope and whole rock Nd and Sr isotopes study of Carboniferous A-type granites, Sierras Pampeanas of Argentina. *J. S. Am. Earth Sci.* **2020**, *100*, 102545. [[CrossRef](#)]
27. Villaseca, C.; Dorado, O.; Orejana, D. Mineral chemistry of megacrysts and associated clinopyroxenite enclaves in the Calatrava volcanic field: Crystallization processes in mantle magma chambers. *J. Iber. Geol.* **2019**, *45*, 401–426. [[CrossRef](#)]
28. Villaseca, C.; García Serrano, J.; Orejana, D. Pyroxenites and megacrysts from alkaline melts of the Calatrava Volcanic Field: Inferences from trace element geochemistry and Sr-Nd isotope composition. *Front. Earth Sci.* **2020**, *8*, 132. [[CrossRef](#)]
29. Ma, S.; Shaw, C.S.J. Vein and wehrlite formation in the lithospheric mantle below the West Eifel Volcanic Field: Modelling the effects of pressure, temperature and peridotite/melt ratio on magma-peridotite interaction using pMELTS and a melt infiltration experiment. *J. Petrol.* **2022**, *63*, egac080. [[CrossRef](#)]
30. Whitney, D.L.; Evans, B.W. Abbreviations for names of rock-forming minerals. *Am. Min.* **2010**, *95*, 185–187. [[CrossRef](#)]
31. McDonough, W.F.; Sun, S.S. The composition of the Earth. *Chem. Geol.* **1995**, *120*, 223–253. [[CrossRef](#)]
32. Bianchini, G.; Beccaluva, L.; Bonadiman, C.; Nowell, G.; Pearson, G.; Siena, F.; Wilson, M. Evidence of diverse depletion and metasomatic events in harzburgite–lherzolite mantle xenoliths from the Iberian plate (Olot, NE Spain): Implications for lithosphere accretionary processes. *Lithos* **2007**, *94*, 25–45. [[CrossRef](#)]
33. Downes, H.; Reichow, M.K.; Mason, P.R.D.; Beard, A.D.; Thirlwall, M.-F. Mantle domains in the lithosphere beneath the French Massif Central: Trace element and isotopic evidence from mantle clinopyroxenes. *Chem. Geol.* **2003**, *200*, 71–87. [[CrossRef](#)]

34. Villaseca, C.; Orejana, D.; Higuera, P.; Pérez-Soba, C.; García Serrano, J.; Lorenzo, S. The evolution of the subcontinental mantle beneath the Central Iberian Zone: Geochemical tracking of its mafic magmatism from the Neoproterozoic to the Cenozoic. *Earth Sci. Rev.* **2022**, *228*, 103997. [[CrossRef](#)]
35. Zindler, A.; Hart, S.R. Chemical geodynamics. *Annu. Rev. Earth Planet. Sci.* **1986**, *14*, 493–571. [[CrossRef](#)]
36. Ionov, D.; Bodinier, J.L.; Mukasa, S.B.; Zanetti, A. Mechanisms and sources of mantle metasomatism: Major and trace element compositions of peridotite xenoliths from Spitsbergen in the context of numerical modelling. *J. Petrol.* **2002**, *43*, 2219–2259. [[CrossRef](#)]
37. Arai, S. Chemistry of chromian spinel in volcanic rocks as a potential guide to magma chemistry. *Mineral. Mag.* **1992**, *56*, 173–184. [[CrossRef](#)]
38. Le Maitre, R.W. *Igneous Rocks: A Classification and Glossary of Terms*; Cambridge University Press: Cambridge, UK, 2002; 236p.
39. Norman, M.D. Melting and metasomatism in the continental lithosphere: Laser ablation ICPMS analysis of minerals in spinel lherzolites from eastern Australia. *Contrib. Mineral. Petrol.* **1998**, *130*, 240–255. [[CrossRef](#)]
40. Galán, G.; Oliveras, V.; Paterson, B.A. Types of metasomatism in mantle xenoliths enclosed in Neogene-Quaternary alkaline mafic lavas from Catalonia (NE Spain). In *Metasomatism in Oceanic and Continental Lithospheric Mantle*; Coltorti, M., Grégoire, M., Eds.; Special Publication 293; Geological Society: London, UK, 2008; pp. 121–153.
41. Avanzinelli, R.; Bianchini, G.; Tiepolo, M.; Jasim, A.; Natalia, C.; Braschi, E.; Dallai, L.; Beccaluva, L.; Conticelli, S. Subduction-related hybridization of the lithospheric mantle revealed by trace element and Sr-Nd-Pb isotopic data in composite xenoliths from Tallante (Betic Cordillera, Spain). *Lithos* **2020**, *352–353*, 105316. [[CrossRef](#)]
42. Beccaluva, L.; Bianchini, G.; Bonadiman, C.; Siena, F.; Vaccaro, C. Coexisting anorogenic and subduction-related metasomatism in mantle xenoliths from the Betic Cordillera (southern Spain). *Lithos* **2004**, *75*, 67–87. [[CrossRef](#)]
43. Shimizu, Y.; Arai, S.; Morishita, T.; Yurimoto, H.; Gervilla, F. Petrochemical characteristics of felsic veins in mantle xenoliths from Tallante (SE Spain): An insight into activity of silicic melt within the mantle wedge. *Earth Environ. Sci. Trans. R. Soc. Edinb.* **2004**, *95*, 265–276.
44. Cebriá, J.M.; López Ruiz, J. Alkali basalts and leucitites in an extensional intracontinental plate setting: The late Cenozoic Calatrava Volcanic Province (Central Spain). *Lithos* **1995**, *35*, 27–46. [[CrossRef](#)]
45. Coltorti, M.; Bonadiman, C.; Hinton, R.W.; Siena, F.; Upton, B.G.J. Carbonatite metasomatism of the oceanic upper mantle: Evidence from clinopyroxenes and glasses in ultramafic xenoliths of Grande Comore, Indian Ocean. *J. Petrol.* **1999**, *40*, 133–165. [[CrossRef](#)]
46. Raffone, N.; Chazot, G.; Pin, C.; Vannucci, R.; Zanetti, A. Metasomatism in the lithospheric mantle beneath Middle Atlas (Morocco) and the origin of Fe- and Mg-rich wehrlites. *J. Petrol.* **2009**, *50*, 197–219. [[CrossRef](#)]
47. Kelemen, P.B.; Shimizu, N.; Salters, V.J.M. Extraction of mid-ocean-ridge basalt from the upwelling mantle by focused flow of melt in dunite channels. *Nature* **1995**, *375*, 747–753. [[CrossRef](#)]
48. Hauri, E.H.; Shimizu, N.; Dieu, J.J.; Hart, S.R. Evidence for hotspot-related carbonatite metasomatism in the oceanic upper mantle. *Nature* **1993**, *365*, 221–227. [[CrossRef](#)]
49. Uenver-Thiele, L.; Woodland, A.B.; Seitz, H.-M.; Downes, H.; Altherr, R. Metasomatic processes revealed by trace element and redox signatures of the lithospheric mantle beneath the Massif Central, France. *J. Petrol.* **2017**, *58*, 395–422. [[CrossRef](#)]
50. Hart, S.R.; Dunn, T. Experimental cpx/melt partitioning of 24 trace element. *Contrib. Mineral. Petrol.* **1993**, *113*, 1–8. [[CrossRef](#)]
51. Foley, S.F.; Jackson, S.E.; Fryer, B.J.; Greenough, J.D.; Jenner, G.A. Trace element partition coefficients for clinopyroxene and phlogopite in an alkaline lamprophyre from Newfoundland by LA-ICP-MS. *Geochim. Cosmochim. Acta* **1996**, *60*, 629–638. [[CrossRef](#)]
52. Zack, T.; Brumm, R. Ilmenite/liquid partition coefficients of 26 trace elements determined through ilmenite/clinopyroxene partitioning in garnet pyroxenites. In Proceedings of the 7th International Kimberlite Conference, Extended abstracts 1988, Cape Town, South Africa, 13–17 April 1998; pp. 986–988.
53. Stoppa, F.; Schiazza, M. An overview of monogenetic carbonatitic magmatism from Uganda, Italy, China and Spain: Volcanologic and geochemical features. *J. S. Am. Earth Sci.* **2013**, *41*, 140–159. [[CrossRef](#)]
54. Xu, Y.G. Evidence for crustal components in the mantle and constraints on crustal recycling mechanisms: Pyroxenite xenoliths from Hannuoba, North China. *Chem. Geol.* **2002**, *182*, 301–322. [[CrossRef](#)]
55. Liu, Y.S.; Gao, S.; Lee, C.T.A.; Hu, S.H.; Liu, X.M.; Yuan, H.L. Melt-peridotite interactions: Links between garnet pyroxenite and high-Mg# signature of continental crust. *Earth Planet. Sci. Lett.* **2005**, *234*, 39–57.
56. Downes, H. Origin and significance of spinel and garnet pyroxenites in the shallow lithospheric mantle: Ultramafic massifs in orogenic belts in Western Europe and NW Africa. *Lithos* **2007**, *99*, 1–24. [[CrossRef](#)]
57. Dantas, C.; Grégoire, M.; Koester, E.; Conceio, R.V.; Rieck, N. The peridotite-websterite xenolith suite from northern Patagonia (Argentina): Evidence of mantle melt reaction processes. *Lithos* **2009**, *107*, 107–120. [[CrossRef](#)]
58. Zhao, X.M.; Cao, H.H.; Mi, X.; Evans, N.J.; Qi, Y.H.; Huang, F.; Zhang, H.F. Combined iron and magnesium isotope geochemistry of pyroxenite xenoliths from Hannuoba, North China Craton: Implications for mantle metasomatism. *Contrib. Mineral. Petrol.* **2017**, *172*, 40. [[CrossRef](#)]
59. Zhao, X.; Wang, H.; Li, Z.; Evans, N.J.; Ying, J.; Yang, Y.; Zhang, H. Nature and evolution of lithospheric mantle beneath the western North China Craton: Constraints from peridotite and pyroxenite xenoliths in the Sanyitang basalts. *Lithos* **2021**, *384–385*, 105987. [[CrossRef](#)]

60. Villaseca, C.; Orejana, D.; Paterson, B.A.; Billström, K.; Pérez-Soba, C. Metaluminous pyroxene-bearing granulite xenoliths from the lower continental crust in central Spain: Their role in the genesis of Hercynian I-type granites. *Eur. J. Mineral.* **2007**, *19*, 463–477. [[CrossRef](#)]
61. Draper, D.S.; Green, T.H. P–T phase relations of silicic, alkaline, aluminous mantle xenolith glasses under anhydrous and C–O–H fluid-saturated conditions. *J. Petrol.* **1997**, *38*, 1187–1224. [[CrossRef](#)]
62. Perinelli, C.; Orlando, A.; Conte, A.M.; Armienti, P.; Borrini, D.; Faccini, B.; Misiti, V.; Coltorti, M.; Grégoire, M. Metasomatism induced by alkaline magma on upper mantle of the Northern Victoria Land (Antarctica): An experimental approach. In *Metasomatism in Oceanic and Continental Lithospheric Mantle*; Coltorti, M., Grégoire, M., Eds.; Special Publication 293; Geological Society: London, UK, 2008; pp. 197–221.
63. Yaxley, G.M.; Kamenetsky, V.; Green, D.H.; Fallon, T.J. Glasses in mantle xenoliths from western Victoria, Australia, and their relevance to mantle processes. *Earth Planet. Sci. Lett.* **1997**, *148*, 433–446. [[CrossRef](#)]
64. Yaxley, G.M.; Kamenetsky, V. In situ origin for glass in mantle xenoliths from southeastern Australia: Insights from trace element compositions of glasses and metasomatic phases. *Earth Planet. Sci. Lett.* **1999**, *172*, 97–109. [[CrossRef](#)]
65. Coltorti, M.; Beccaluva, L.; Bonadiman, C.; Salvini, L.; Siena, F. Glasses in mantle xenoliths as geochemical indicators of metasomatic agents. *Earth Planet. Sci. Lett.* **2000**, *183*, 303–320. [[CrossRef](#)]
66. Bowman, E.E.; Ducea, M.N. Pyroxenite melting at subduction zones. *Geology* **2023**, *51*, 383–386. [[CrossRef](#)]
67. Su, B.X.; Zhang, H.F.; Sakyi, P.A.; Zhang, Y.H.; Ying, J.F.; Tang, Y.J.; Qin, K.Z.; Xiao, Y.; Zhao, X.M.; Mao, Q.; et al. The origin of spongy texture in minerals of mantle xenoliths from the Western Qinling, Central China. *Contrib. Mineral. Petrol.* **2011**, *161*, 465–482. [[CrossRef](#)]
68. Pan, S.; Zheng, J.; Yin, Z.; Griffin, W.L.; Xia, M.; Lin, A.; Zhang, H. Spongy texture in mantle clinopyroxene records decompression-induced melting. *Lithos* **2018**, *320–321*, 144–154. [[CrossRef](#)]
69. Shaw, C.S.J.; Dingwell, D.B. Experimental peridotite-melt reaction at one atmosphere: A textural and chemical study. *Contrib. Mineral. Petrol.* **2008**, *155*, 199–214. [[CrossRef](#)]
70. Rielli, A.; Tomkins, A.G.; Nebel, O.; Brugger, J.; Etschmann, B.; Evans, K.A.; Wykes, J.L.; Vasyliov, P.; Paterson, D.J. Incipient metal and sulfur extraction during melting of metasomatised mantle. *Earth Planet. Sci. Lett.* **2022**, *599*, 117850. [[CrossRef](#)]
71. Picazo, S.; Müntener, O.; Manatschal, G.; Bauville, A.; Karner, G.; Johnson, C. Mapping the nature of mantle domains in Western and Central Europe based on clinopyroxene and spinel chemistry: Evidence for mantle modification during an extensional cycle. *Lithos* **2016**, *266–267*, 233–263. [[CrossRef](#)]
72. Puziewicz, J.; Matusiak-Malek, M.; Ntaflos, T.; Grégoire, M.; Kaczmarek, M.-A.; Aulbach, S.; Ziobro, M.; Kukula, A. Three major types of subcontinental lithospheric mantle beneath the Variscan orogen in Europe. *Lithos* **2020**, *362–363*, 105467. [[CrossRef](#)]
73. González-Jimenez, J.M.; Villaseca, C.; Griffin, W.L.; Belousova, E.; Konc, Z.; Ancochea, E.; O’Reilly, S.Y.; Pearson, N.J.; Garrido, C.J.; Gervilla, F. The architecture of the European-Mediterranean lithosphere: A synthesis of the Re-Os evidence. *Geology* **2013**, *41*, 547–550. [[CrossRef](#)]

**Disclaimer/Publisher’s Note:** The statements, opinions and data contained in all publications are solely those of the individual author(s) and contributor(s) and not of MDPI and/or the editor(s). MDPI and/or the editor(s) disclaim responsibility for any injury to people or property resulting from any ideas, methods, instructions or products referred to in the content.